Thermal expansion of the Al_2SiO_5 polymorphs, kyanite, andalusite and sillimanite, between 10 and 1573 K determined using time-of-flight neutron powder diffraction

A. Dominic Fortes

Published version information

Citation: AD Fortes. "Thermal expansion of the Al_2SiO_5 polymorphs, kyanite, andalusite and sillimanite, between 10 and 1573 K determined using time-of-flight neutron powder diffraction." Physics and Chemistry of Minerals, vol. 46, no. 7 (2019): 687-704.

DOI: https://doi.org/10.1007/s00269-019-01031-3

Thermal expansion of the Al_2SiO_5 polymorphs, kyanite, andalusite and sillimanite, between 10 and 1573 K determined using time-of-flight neutron powder diffraction.

A. Dominic Fortes,[1,2,†]

[1]ISIS Facility, STFC Rutherford Appleton Laboratory, Harwell Science and Innovation Campus, Chilton, Didcot, Oxfordshire, OX11 0QX, U.K.
[2]Department of Earth Sciences, University College London, Gower Street, London WC1E 6BT, U.K.

Corresponding author email dominic.fortes@stfc.ac.uk

Synopsis

High-resolution neutron powder diffraction measurements on kyanite, andalusite and sillimanite as a function of temperature substantially improve our knowledge of their thermal expansion, both in terms of precision and revealing hitherto unknown behaviour in these materials, such as negative linear expansion.

Abstract

Powder and single-crystal diffraction data measured from the three geologically important Al_2SiO_5 polymorphs, kyanite, andalusite and sillimanite, over the last six decades have given varying accounts of each polymorph's thermal expansion; the scatter between and even within experimental datasets is often quite large, Furthermore, there are no lattice parameter determinations below 273 K, where the thermodynamic functions vary substantially, and few measurements above 1200 K.

Accurate and precise lattice parameters of natural kyanite, andalusite and sillimanite have therefore been obtained in the range 10 to 1573 K using the High-Resolution Powder Diffractometer (HRPD) at the ISIS neutron spallation source. Accuracy is ensured by the use of an internal standard (NIST silicon SRM640c) and use of a bulk probe (neutrons) in order to avoid the specimen-displacement corrections required by typical back-reflection X-ray diffraction methods. Precision is ensured by use of the time-of-flight method on one of the longest primary neutron flightpath instruments in the world.

For kyanite, the improved precision reveals the true temperature-dependence of the three inter-axial angles for the first time, permitting derivation of accurate thermal expansion tensor coefficients. For both andalusite and sillimanite, the measurements reveal hitherto unknown regions of substantial negative linear expansivity below room temperature, along the *c*-axis in andalusite and along the *a*-axis in sillimanite. Above 1200 K, sillimanite exhibits an anomalous increase in thermal expansion that may be due to a change in the Al/Si tetrahedral site ordering.

Keywords

Al_2SiO_5, Kyanite, Andalusite, Sillimanite, thermal expansion, neutron diffraction

1. Introduction

Al_2SiO_5 crystallises in three naturally-occurring polymorphs, kyanite ($P\bar{1}$), andalusite (*Pnnm*) and sillimanite (*Pbnm*) depending on the formation pressure and temperature (Burnham & Buerger, 1961; Burnham, 1963a, 1963b; Finger & Prince, 1972; Kerrick, 1990). Each polymorph is characterised by edge-sharing AlO_6 octahedra forming chains that extend along the *c*-axis, which are cross-linked by chains of silica-alumina polyhedra (Figure 1). In kyanite, the chains comprise alternating SiO_4–AlO_6; in andalusite they are alternating SiO_4–AlO_5; in sillimanite they are alternating SiO_4–AlO_4. Although a very small degree of Al/Si site substitution occurs naturally in such minerals (e.g., Gatta et al., 2009), sillimanite differs from kyanite and andalusite in that the fully-ordered chains of Si–Al–Si–Al tetrahedra present at low temperature (Stebbins et al. 1993) start to become disordered above ~ 1200 K (Igami et al., 2018).

Figure 1

These three minerals are produced by varying degrees of metamorphism of pelitic sedimentary rocks, the phase-assemblage produced being diagnostic of the 'peak' P/T conditions (e.g., Ghent, 1976; Newton & Haselton, 1981; Ghent et al., 1982: Koziol & Newton, 1988; Ghent & Grover, 1995). Metamorphic petrologists use them to establish the depths and rates of tectonic burial and exhumation (e.g., Tropper & Hoinkes, 1996; Barnhart et al., 2012) and the accuracy of this geological tool thus depends on how well the material's behaviour is known as a function of pressure and temperature. Since the Al_2SiO_5 polymorphs are the most common and well-known low-grade geothermometers and geobarometers, there have been extensive experimental and computational efforts devoted to quantifying the thermodynamic properties of these three minerals (e.g., Neumann, 1925; Brace et al., 1969; Comodi et al., 1997; Friedrich et al., 2004; Liu et al., 2009; Oganov & Brodholt, 2000; Schmidt et al., 1997; Winkler, 2001).

An important facet of the thermodynamic studies is accurate and precise determination of the thermal expansion. All of the thermal expansion studies on these materials carried out to date have been made at temperatures ≥ 273 K and (with few exceptions) using X-ray powder diffraction methods (Skinner et al., 1961; Winter & Ghose, 1979; Schneider, 1979; Hemingway et al., 1991; Liu et al., 2010; Hu et al., 2011). Gatta et al. (2006) used angle-dispersive neutron

powder diffraction to characterise the thermal expansion of kyanite in the range 600 – 1473 K, with one additional room-temperature observation.

The consequences of this are two-fold: Firstly, the measurements above room-temperature are made in the region where the thermal expansion varies little and (roughly) linearly. This is convenient inasmuch as one can parameterise the temperature dependence of the molar volume with simple polynomials, which then clearly have no predictive value outside the fitting range. Indeed, it remains common practice to treat the thermal expansion above room temperature as a constant (e.g., He et al., 2016). Secondly, the result of using angle-dispersive diffraction is the need to measure to high 2θ in order to obtain the highest precision on the cell parameters and to refine systematic peak shifts due to thermal expansion of the specimen surface and substrate. Whilst many workers go to great lengths to apply accurate corrections, it is often the case that fitting will be done only to comparatively low angles ($< 90°$ 2θ) or using a selection of peaks in a narrow range. In the case of the triclinic polymorph, kyanite, it is quite clear from the literature data (as comparisons shown later will demonstrate) that no-one has yet satisfactorily corrected for the systematic temperature-dependent aberrations that affect X-ray powder measurements or achieved the requisite level of precision; particularly for the angles α, β and γ, where the variations with temperature are small and the observations are highly scattered.

Application of a bulk neutron probe is useful to avoid the thermal expansion-related corrections implicit in X-ray powder diffraction analyses, and the time-of-flight method on a long flight-path instrument with very high 2θ detectors is crucial to achieve the requisite precision on the thermal expansion tensor coefficients. The objectives of this work are thus to carry out measurements at the highest level of accuracy and precision for all three polymorphs using the same diffractometer, sample-environment and thermal protocols, and to do so from close to absolute zero temperature up to the region where decomposition or other structural changes may occur. This strategy allows for observation of new behaviour outside the limits that have hitherto been explored, better distinction of subtleties in regions that have been measured previously, and the most reliable comparative analysis between the polymorphs.

2. Experimental methods

2.1 Sample characterisation

Specimens of 'gem quality' kyanite, andalusite and sillimanite were obtained from various internet vendors; the exact provenance of each mineral is not known but the source localities were reported to be Nepal (kyanite), Bazil (andalusite) and Sri Lanka (sillimanite). The kyanite and andalusite samples were supplied in the form of flat circular beads. Kyanite samples exhibited colour variations between white and dark blue, and the andalusite samples varied from pale pink, through brown to a smoky green colour. Stones were selected for experimental analysis on the basis of uniform colour and lack of visible inclusions. By contrast, all of the sillimanite specimens were a uniform lemon yellow colour, of high transparency and free of inclusions, being supplied in faceted peardrop shapes. Samples of each mineral were embedded in resin, polished, carbon-coated and then analysed for major elements using a JEOL JXA8100 microprobe. The average of twenty point-analyses are reported in Table 1. Each is close to the ideal Al_2SiO_5 chemical composition (62.93 wt % Al_2O_3, 37.07 wt % SiO_2) with iron being the only significant and substantial substituent. The occurrence of almost 1 % FeO in the sillimanite crystals is consistent with their yellow colouration (Rossman et al. 1982).

Table 1

Initial phase identification was done using Raman spectroscopy. Data were acquired in the range 80–4000 cm^{-1} following excitation with 532 nm laser light using a B&WTek *i*-Raman Plus spectrometer; the dark-subtracted spectra are shown in Supplementary Figure S1 along with reference spectra from the RRUFF library (Lafuente et al., 2015). There are substantial difference between the spectra of all three Al_2SiO_5 polymorphs, making Raman spectroscopy a very quick and unambiguous diagnostic tool in this instance; it is clear that there is excellent agreement between the library spectra and those measured from the samples used in this work.

2.2 Neutron powder diffraction

Neutron powder diffraction data (Fortes, 2016) were collected using the High Resolution Powder Diffractometer (HRPD) (Ibberson *et al.,* 1992: Ibberson, 2009) at the STFC ISIS spallation neutron source, Rutherford Appleton Laboratory, UK. Specimens were pulverized in a percussion mortar, followed by gentle grinding under acetone in an agate mortar, until all material passed through a 150 μm sieve. Due to the limited quantity of inclusion-free kyanite and andalusite, smaller samples and longer measurement times were used, as detailed below.

For the low-temperature analysis, the sample holder consisted of an aluminium-alloy frame with a slab-geometry space of dimensions (relative to the incident beam) of width = 18 mm, height = 23 mm and depths of 5 mm (kyanite and andalusite) or 10 mm (sillimanite). These holders have holes drilled either side of the specimen, one to accept a RhFe resistance thermometer, fully calibrated on the ITS-1990 scale, and the other to take a cartridge heater (Watlow Firerod C1E-192). The open front and back faces of the holder are covered with 125 μm-thick vanadium foil windows, sealed in place with steel frames and indium wire. Exposed steel and Al surfaces on the front of the sample holder are masked from the incident beam with Gd and Cd foils.

Samples were loaded into a closed-cycle refrigerator (CCR) at ~ 250 K and then cooled *in situ* to 10 K immersed in 50 – 100 mbar of helium exchange-gas. Following an initial measurement of 1 hr duration at 10 K, the samples were warmed in 10 K increments up to 200 K and 20 K steps thereafter to > 400 K. The highest temperatures measured in the CCR were 460 K for kyanite, 420 K for andalusite and 440 K for sillimanite. Equilibration times at each datum were 10 minutes, followed by counting times of 30 min for kyanite and andalusite, and 15 min for sillimanite.

Additional samples, mixed with NIST silicon powder (Standard Reference Material 640c), were prepared and loaded into Al-framed slab cans. These were measured at the standard reference temperature of 22.5 °C (295.65 K) and at a range of temperatures that would ensure calibrated overlap between low- and high-temperature datasets. For kyanite this range was 250 – 370 K, for andalusite 290 – 450 K, and for sillimanite 290 – 370 K.

For the high-temperature analysis, the sample holder consisted of a vanadium-foil tubular canister with a diameter of 11 mm. These were filled to a depth of at least 20 mm (the beam height at the sample) and attached to mounting sticks with tungsten wire. Two S-type thermocouples were secured to the either side of the sample can with their tips ~ 1 cm above the top of the sample.

These were loaded into the ISIS 'Risø' furnace at room temperature (291 – 292 K), pumped down to a high vacuum (10^{-6} mbar), and then heated using vanadium-foil elements. Samples were initially heated to 373 K for at least 1 hr to promote outgassing. Measurements were then made in 50 K increments from 423 – 1573 K, the maximum working temperature of the furnace in this configuration being ~ 1623 K, counting for 30 minutes with 10 minutes of thermal equilibration for both kyanite and sillimanite. Counting times for andalusite were increased to 1 hr in order to ensure comparable statistics. Whilst both andalusite and sillimanite were

unaltered by heating to 1573 K, kyanite underwent a partial transformation during the course of the final measurement to a mixture containing ~ 34.3 wt % of the 3:2 mullite phase, in agreement with literature observations (e.g., Barlett, 1940; Sainz et al., 1997; Kaschcheev et al., 2007). Figure 2 shows some representative segments of the high-temperature data for each polymorph, which illustrate both the partial transformation of kyanite at 1573 K (Figure 2a) and the clear difference in anisotropic shifts of the Bragg peaks between the three polymorphs, indicative of the large variations in thermal expansion anisotropy.

Figure 2

Diffraction data at all temperatures were collected in HRPD's standard 100 ms-wide time-of-flight window in the range 30 – 130 ms (corresponding to d-spacings of 0.65 – 2.60 Å in the instrument's backscattering detector banks), normalised to the incident spectrum and corrected for instrument efficiency by reference to a V:Nb standard using the Mantid library of diffraction algorithms (Mantid, 2013: Arnold et al., 2014).

3. Results

3.1 Profile refinement

A total of sixty-six data points were obtained for kyanite, sixty-six for andalusite and, due to time constraints, sixty-one for sillimanite. Analysis of the neutron powder diffraction data at each of these state points was done with GSAS/Expgui (Larsen & Von Dreele, 1994: Toby, 2001). Whilst the diffraction patterns of all specimens were found to be free of contaminants and the Bragg peaks were very sharp, all three of the Al_2SiO_5 polymorphs exhibited some degree of preferred orientation as a result of being packed into their respective sample holders. Further quantitative detail concerning the texture of each sample is provided in Supplementary Tables S1 and S2 and Figure S2. Consequently, the analysis in GSAS was carried out with the "F(calc) Weighted" model, which uses structure factors from a calculated model only as a starting point, allowing these to vary independently in subsequent refinement cycles. This yields better precision on the lattice parameters (the main goal of this work) by more accurately fitting the intensities. Example diffraction datasets and profile refinements for each phase are shown in Figure 3.

Figure 3.

Where it was essential to refine phase fractions (e.g., kyanite + mullite at 1573 K) or to try and obtain insight into site ordering (e.g, sillimanite above 1200 K), then models were fitted using the Rietveld method employing the spherical-harmonic texture models implemented in GSAS (Supplementary Table S1). The refinement work-flow commenced with the specimens mixed with NIST silicon powder, measured at 295.65 K; the instrumental parameters DIFC and DIFA, defining the neutron flight path and the wavelength dependent absorption from the sample respectively, were refined, along with the lattice parameters of each Al_2SiO_5 polymorph whilst the lattice constant of silicon was kept fixed at the certified reference value of 5.431195 Å. Subsequently, the DIFC term was refined in the low-temperature and high-temperature silicon-free datasets in order to achieve the closest agreement in Al_2SiO_5 polymorph lattice parameters with the silicon-calibrated values. The congruity between the three datasets for each polymorph is shown graphically in Supplementary Figure S3–S5.

The refined lattice parameters are tabulated in the electronic supplement to this article, Tables S3–S5. A comparison of my results with the literature data for kyanite, andalusite and sillimanite are shown, respectively, in Figures 4, 5 and 6.

Figures 4, 5 and 6

3.2 Analysis of the thermal expansion

A variety of physically meaningful functional forms may be used to fit the temperature variation of lattice parameters as a function of temperature, including models based on Debye-type or Einstein-type descriptions of the material's vibrational density of states. Where specific heat measurements are available, it is usually desirable to fit these to obtain the characteristic Debye / Einstein cut-off frequencies, or temperatures, and to then keep these fixed whilst optimising other variables to fit the thermal expansion. As detailed in the supplementary material, a three-term Debye model of each polymorph's internal energy was derived from a fit to literature heat capacity data, shown in Figure S6 (Pancratz & Kelley, 1964; Robie & Hemingway, 1984; Salje, 1986; Hemingway et al., 1991). Augmented with empirical determinations of each polymorph's bulk modulus (Yang et al., 1997a, 1997b; Burt et al., 2006), an excellent fit of this model to the temperature dependence of the molar volumes was obtained. However, these models employ a large number of parameters and cannot

independently and uniquely constrain the material properties of interest. They nevertheless demonstrate consistency with the extant data on the vibrational and elastic characteristics of each polymorph (Tables S6 and S7). Because a comprehensive discussion of the Debye models is of indirect interest, the details appear only in the electronic supplement to this paper.

Since the Debye-type models of thermal expansion are also (*i*) fairly complex and (*ii*) only dimensionally correct for the volume, I have adopted a much simpler and more general approach to fitting the individual lattice parameters. Here I will show that the temperature dependence of the lattice parameters may be fitted accurately with simple functions described by just a few variable quantities.

For all parameters except β and γ in kyanite, I have fitted an expression of the following form;

$$X = X_0 + \frac{S}{(e^{1/T} - 1)} \tag{1}$$

where X_0 is the value of the parameter at T = 0 and S is a sigmoidal function, the exact nature of which is determined from the experimental data. For almost all parameters, it was found that S was well represented by a power law;

$$S = A = a \cdot T^{b/T} \tag{2}$$

However, there were specific instances where the curvature was better fitted by an exponential or a hyperbolic tangent function;

$$S = B = c \cdot e^{d/T} \tag{3}$$

$$S = C = a(1 - \tanh(b/T)) \tag{4}$$

Naturally, to fit those cell parameters exhibiting regions of substantial negative expansivity required a linear combination of these functions;

$$S = A + B = \left[\left(a \cdot T^{b/T}\right) + \left(c \cdot e^{d/T}\right)\right] \tag{5}$$

Finally, the two inter-axial angles, β and γ in kyanite, which exhibited only very small variations with temperature, were fitted with simple polynomials;

$$X = X_0 + aT + bT^2 \quad (6)$$

Non-linear least-squares unweighted fitting of these equations to the experimental data were done in DataFit (Oakdale Engineering) and the parameters are listed in Tables 2, 3 and 4 with explicit identification of which functional form of S was used for each fit. The solid lines in Figures 4, 5 and 6 depict these fits graphically. Since an accurate reproduction of these curves may depend on more digits than are consistent with the parameter's uncertainty, these additional digits are provided in Supplementary tables (S8–S10).

Tables 2, 4 and 5

3.3 Determination of thermal expansion tensors

The six independent expansion coefficients for triclinic kyanite (Figure 7) and the three linear thermal expansion coefficients for orthorhombic andalusite (Figure 8) and sillimanite (Figure 9), were obtained from the 'raw' refined unit-cell parameters and from the fitted curves as follows. Eulerian infinitesimal strain tensors were calculated from pairs of cell parameters and then normalised by the thermal increment between them in order to obtain thermal expansion tensors, i.e., unit-strain tensors (*cf*., Hazen et al., 2000). Larger error bars at high temperature arise from the intrinsically lower precision of the high-*T* lattice parameter refinements, which is typical for any material, whereas the larger error bars at low temperature are a manifestation of the small temperature increments used.

For kyanite, standard matrix decomposition methods (e.g., Abdi, 2007) were used to derive the eigenvalues and eigenvectors of the thermal expansion tensor, these being the magnitudes and orientations of the principal expansivities. Figure 10 compares the volume thermal expansion of each polymorph, obtained from the lattice-parameter fits, and Figure 11 compares the linear expansivities in the same manner.

Figures 7, 8 and 9

Figures 10 and 11

The principal directions of the thermal expansion tensors in andalusite and sillimanite are constrained by symmetry to coincide with the lattice vectors; hence the principal magnitudes of the expansion tensor, α_i, correspond with the linear expansivities of the unit-cell edges. The thermal expansion tensor in kyanite has no such symmetry constraints, and a convenient representation of how the principal directions relate to the structure and how they vary with temperature is more challenging to report. Figure 12 shows sections of the tensor representation surface perpendicular to *a**, *b* and *c* in the form of temperature contours. Representation glyphs (*cf.*, Hashash et al. 2003) are shown in the middle of Fig. 12, corresponding with the thermal expansion at 1500 K, including arrows to indicate both the unit cell and the principal directions. Views of the kyanite structure in the same set of orientations appear on the right of Figure 12. In order to provide a direct comparison with the study by Gatta et al. (2006), Figure 13 shows strain ellipsoids projected directly onto the structure of kyanite and viewed along α_1 and α_2.

Figures 12 and 13

4. Discussion

It is clear from examination of the scatter of experimental data points in Figures 4, 5 and 6 that the systematic errors in this work are sufficiently small to obtain accurate temperature dependences, even for parameters such as the triclinic angles in kyanite where the variation is very small. This contrasts with the larger systematic errors (and thus greater scatter) in the various datasets obtained by angle-dispersive diffraction. Liu et al. (2010) commented that kyanite's inter-axial angles exhibited a "complicated variation pattern" and that this was due to the "low symmetry … and large unit-cell parameters." However, it is plain from Figure 4 that the pattern of variation is actually very simple and smooth; the purported 'complexity' of the earlier measurements arises from systematic errors that are considerably greater than might be inferred from the reported error bars. This is due to the use of only 66 reflections at low 2θ (10 – 43°) by Liu et al., compared with > 2500 reflections measured at high 2θ (154 – 176°) in this work. Evidently, time-of-flight neutron diffraction with a long primary flight-path and fixed detectors at high backscattering angles is a method perfectly suited to these types of problems involving minerals of low-symmetry with small variations of lattice parameters in *T*

and *P*. Nevertheless, it is worth saying that the work by Hu et al. (2011) is very good, showing the closest agreement with these results.

Since lattice parameters were measured from all three polymorphs, mixed with a silicon standard under at least two identical temperature conditions, it is possible to report the most accurate values for the differences in molar volume, ΔV. My values of the molar volume and volume differences at 295.65 K are compared with literature values in Table 5. Further determination of the temperature dependencies of ΔV, based on the high and low-*T* datasets that have been calibrated where they overlap with the silicon mixtures, are shown in Supplementary Figure S7. The volume difference between andalusite and kyanite, and between andalusite and sillimanite, each increase with temperature; the volume difference between sillimanite and kyanite has a negative temperature dependence.

Table 5

Despite the much improved precision, the general form of the thermal expansion of each polymorph between 300 and 1200 K is not dramatically different from earlier studies. However, the measurements outside this range are new and reveal interesting features worthy of discussion, such as the negative linear expansion observed at low temperatures in andalusite and sillimanite (Figure 14), and the anomalous changes in linear expansion of sillimanite at high temperature.

Figure 14

The negative linear expansion in andalusite is parallel to the *c*-axis, coinciding with the chains of alternating SiO_4–AlO_6 polyhedra shown in Figure 1; α_c turns negative below ~265 K, reaching a minimum value of $-1.50\text{x}10^{-6}$ K^{-1} at ~125 K. Due to the rapid low-temperature rise of both α_a and α_b, there is no discernible region of negative *volume* expansion in andalusite. By contrast, the negative linear expansion in sillimanite is parallel to the *a*-axis. Figure 15 shows a view of the structure in the *a*–*b* plane; the canted bow-tie shapes are the projected geometries of the SiO_4–AlO_4 chains running parallel with the *c*-axis, viewed end-on, whilst the cross-linking AlO_6 octahedra are shown in faint. The principal difference between the *a*- and *b*-direction is in the orientation of the AlO_6 octahedron's long axis.

Figure 15

In sillimanite, α_a turns negative below ~275 K, reaching a minimum value of $-1.27\text{x}10^{-6}$ K^{-1} at ~ 120 K. Unlike andalusite, the expansion of the other two directions – in particular along the *c*-axis – is small with a delayed rise, leading to a region in which the negative expansion along the *a*-axis dominates and thus becomes manifested in the volume expansivity. Hence there appears to be, at the edge of statistical certainty, a region of negative α_V below ~ 90 K, reaching a minimum value of around $-5\text{x}10^{-7}$ K^{-1} close to 50 K.

One would expect the origin of the negative expansion to be low-frequency vibrational modes, ν_i, with negative mode Grüneisen parameters, $\gamma_i = \partial\nu_i/\partial V$. Remarkably, such modes were reported in sillimanite nearly 30 yr ago by Murnagh & Liu (1991). Their measurements of the pressure-dependence of Raman-active modes found Grüneisen parameters of −0.48(5) for the peak observed (at zero *P*) at 311 cm^{-1} and $\gamma = -0.92(9)$ for the Raman peak at 236 cm^{-1}. In my triple-Debye-model fit to the unit-cell volume of sillimanite, described in the electronic supplement, the fit parameter *X* that pertains to the lowest Debye temperature (θ_{D1} = 498 K, corresponding to a cut-off frequency of 346 cm^{-1}) has a weakly negative value (Supplementary Table S7); since *X* is inversely proportional to the Grüneisen parameter for the vibrational modes up to the θ_{D1} cut-off, the fit confirms that this Grüneisen parameter is also negative, in agreement with the observations of Murnagh & Liu (1991). These vibrations correspond with rotational and translational modes of the tetrahedra, in respect of which it was noted by Iishi et al. (1979) and Salje & Werneke (1982) that the irregular nature of the AlO_5 polyhedra in andalusite works to harden the structure against rotational motion as compared with the more regular AlO_4 tetrahedra in sillimanite. Thus, the lower barrier to rotational modes in sillimanite – modes with negative Grüneisen parameters – may be the reason they can exert a greater influence at low temperatures in sillimanite and so produce the observed negative linear expansion.

It is worth adding the caveat that Murnagh and Liu (1991) reported no modes with negative Grüneisen parameters in andalusite, leaving the origin of the negative expansion along that polymorph's *c*-axis unclear for the present.

At temperatures > 1200 K in sillimanite, it is clear simply by examination of the axial ratios (Figure 6) that the linear expansivities deviate from the low-temperature trend. For the models fitted to lattice parameters measured below 1200 K, I find therefore that both α_a and α_b increase at a faster rate and α_c decreases with respect to the low-*T* behaviour, leading to a

large net increase in α_V (Figure 9). There are no obvious changes in the intensity or width of Bragg peaks in the raw diffraction data that might hint at a substantial structural alteration and neither do I observe any new peaks indicative of a phase transition or decomposition. One plausible explanation is the onset of disorder in the SiO_4–AlO_4 chains. At low temperatures, these are expected to be fully ordered (as depicted in Figure 1), with a transition to a fully-disordered state (involving a halving of the *c*-axis length and a change in space group from *Pbnm* to *Pbam*) at temperatures of ~ 2000 K (e.g., Greenwood, 1972; Guse et al., 1979). Holland and Carpenter (1986) observed such disordered crystals following annealing of sillimanite at temperatures of 1953 – 1963 K under confining pressures of 18 – 20 kbar. Nevertheless, there is every reason to expect that *partial* disorder should occur at lower temperatures whilst retaining *Pbnm* symmetry and efforts to characterise this experimentally and computationally have been made (Bish & Burnham, 1992; Stebbins et al. 1993; Bertram et al., 1990). Bish & Burnham reported neutron powder diffraction data, from which they refined a substantial degree of site disorder (18 %). Later analysis of ^{29}Si NMR data by Stebbins et al. (1993) showed that the Al/Si tetrahedral sites actually had a high degree of local order and suggested that the origin of the disagreement with the diffraction data was the presence of a kind of stacking disorder *between* chains that were themselves completely ordered (*cf*., Lefebvre & Paquet, 1983).

These remarks are pertinent because Rietveld refinement of my sillimanite data show, firstly that at 373 K there is a high degree of apparent Al/Si tetrahedral site disorder, 20.0(5) %, and secondly that this is barely statistically-significantly different at 1573 K, being 18.0(6) %. Consequently, it seems probable that (like earlier workers) we are observing the effect of chain disorder and that any slight decrease at high temperature may reflect a degree of annealing of the stacking disorder rather than any change in the true local order. Indeed, Bertram et al. (1990) calculated the effect of Al/Si tetrahedral site disorder on the lattice parameters, determining that the *a*-axis and *b*-axis should shrink and the *c*-axis should expand on disordering. This is exactly the reverse of what I observe, perhaps lending weight to an interpretation of the anomalous expansion in terms of annealed stacking disorder rather than local partial disordering.

Conversely, the calculations of Bertram et al. (1990) may not be wholly accurate. Igami et al. (2018) used a novel X-ray spectroscopic method to obtain Al/Si site occupancies in sillimanite annealed at high-temperatures, showing that there is indeed a decrease in the order parameter between 1273 and 1873 K, with an estimated transition temperature to a fully

disordered state of 2000 K, in good agreement with Greenwood's (1972) statistical calculation. It is therefore possible that the expansion anomaly at 1200 K marks the onset of *partial* disordering and the disagreement between my observations and the calculations of Bertram et al. (1990) reflects a deficiency of their computational model.

In either case, it is improbable that the lattice parameters measured here reflect an equilibrium configuration of partially-ordered tetrahedral sites or partially-ordered chains since the experimental time available was naturally quite short compared with the likely kinetics of the ordering process. Note that Igami et al. (2018) annealed their specimens for periods of 90 – 1500 hr prior to making their measurement.

5. Concluding remarks

I have measured high-resolution powder diffraction data over the widest range of temperatures yet reported for the three Al_2SiO_5 polymorphs, kyanite, andalusite and sillimanite, yielding refined lattice parameters of substantially better accuracy and precision than any preceding study, showing in the process that even simple and well-studied materials often have unexpected and interesting information to impart. Both andalusite and sillimanite exhibit hitherto unknown regions of negative linear expansion below room temperature and sillimanite has thermal expansion anomalies above 1200 K that may be due to Al/Si site disordering. So as to capitalise on these new data, it would be beneficial to measure the elastic properties of all three minerals below room temperatures and to extend the thermal expansion measurements on sillimanite above 1573 K, perhaps also using total-scattering methods in order to better understand changes in local structure and giving due consideration to the use of extended annealing times in order to more closely approach an equilibrium condition. To the best of my knowledge there has been no measurement of the elastic properties of andalusite and sillimanite below room-*T* and only calculations of the elastic constants of kyanite (e.g., Vaughn & Weidner, 1978; Winkler et al., 2001; Page & Saxe, 2002; Yao et al., 2007). Careful evaluation of the vibrational modes leading to the observed negative linear expansion in andalusite and sillimanite should be done, most profitably using computational methods.

Acknowledgements

Neutron diffraction work was supported by a beam-time allocation from the STFC ISIS Facility (RB 1620003, doi:10.5286/ISIS.E.83382292). The author thanks Dr Andrew Beard (Birkbeck,

University of London) for collection of microprobe measurements, and Paul McIntyre and Adam Sears (Rutherford Appleton Laboratory) for their assistance with the high-temperature portion of this work. G. D. Gatta and one anonymous referee are thanked for their comments on the manuscript.

References

Abdi H (2007) The eigen decomposition; eigenvalues and eigenvectors. In, Encylopedia of Measurements and Statistics (N J Salkind, Ed), Sage Publications, Thousand Oaks, California.

Arnold O, & 27 co-authors (2014) Mantid—Data analysis and visualization package for neutron scattering and μSR experiments. Nucl Instrum Methods Phys Res A 764: 156–166.

Barlett H B (1940) Rate of decomposition of kyanite at various temperatures. J Am Ceram Soc 23: 249–251.

Barnhart K R, Walsh P J, Hollister L S, Daniel C G, Andronicos C L (2012) Decompression during Late Proterozoic Al_2SiO_5 triple-point metamorphism at Cerro Colorado, New Mexico. J Geol 120: 385–404.

Brace W F, Schulz C H, La Mori P N (1969) Isothermal compressibility of kyanite, andalusite, and sillimanite from synthetic aggregates. J Geophys Res 74: 2089–2098.

Burnham C W (1963a) Refinement of the crystal structure of sillimanite. Z Krist 118: 127–148.

Burnham C W (1963b) Refinement of the crystal structure of kyanite. Z. Krist. 118: 337–360.

Burnham C W, Buerger M J (1961) Refinement of the crystal structure of andalusite. Z Krist 115: 269–290.

Burt J B, Ross N L, Angel R J, Koch M (2006) Equations of state and structures of andalusite to 9.8 GPa and sillimanite to 8.5 GPa. Am Mineral 91: 319–326.

Comodi P, Zanazzi P F, Poli S, Schmidt M W (1997) High-pressure behaviour of kyanite: Compressibility and structural deformations. Am Mineral 82: 452–459.

Finger L W, Prince E (1972) Neutron diffraction studies: andalusite and sillimanite. Carnegie Institution of Washington, Year Book: 71: 496–500.

Fortes A D (2016) *Thermal expansion of kyanite, andalusite and sillimanite*, 1620003, STFC ISIS Facility, doi:10.5286/ISIS.E.83382292

Friedrich A, Kunz M, Winkler B, Le Bihan T (2004) High-pressure behaviour of sillimanite and kyanite: compressibility, decomposition and indications of a new high-pressure phase. Z Krist 219: 324–329.

Gatta G D, Nestola F, Walter J M (2006) On the thermo-elastic behaviour of kyanite: a neutron powder diffraction study up to 1200 °C. Mineral Mag 70: 309–317.

Gatta G D, Rotitoti N, Zucali M (2009) Plastic deformation in kyanites by tectonometamorphic processes: a single-crystal X-ray diffraction study. Mineral Mag 73: 359–371.

Ghent E D (1976) Plagioclase-garnet-Al_2SiO_5-quartz: a potential geobarometer-geothermometer. Am Mineral 61: 710–714.

Ghent E D, Grover T W (1995) Calculation of the activity of Al_2SiO_5; applications to the geobarometry and geohygrometry of garnet and staurolite zone metapelitic rocks. Am J Sci 295: 923–942.

Ghent E D, Knitter C C, Raeside R P, Stout M Z (1982) Geothermometry and geobarometry of pelitic rocks, upper kyanite and sillimanite zones, Mica Creek area, British Columbia, Canadian Mineral 20: 295-305

Greenwood H J (1972) Al^{IV}-Si^{IV} disorder in sillimanite and its effect on phase relations of the aluminum silicate minerals. Mem Geol Soc Am 132: 553–571.

Guse W, Saalfeld H, Tjandra, J (1979) Thermal transformations of sillimanite single crystals. Neues Jahrb Min Monat 175–181.

Hashash Y M A , Yao J I –C, Wotring D C (2003) Glyph and hyperstreamline representation of stress and strain tensors and material constitutive response. Int J Num Anal Methods Geomech 27: 604–626.

Hazen R M, Downs R T, Prewitt C T (2000) Principles of comparative crystal chemistry. Rev Mineral Geochem 41: 1–33.

He Q, Liu X, Li B, Deng L, Liu W, Wang L (2016) Thermal equation of state of a natural kyanite up to 8.55 GPa and 1273 K. Matter and Radiation at Extremes 1: 269–276.

Hemingway B S, Robie R A, Evans H T, Kerrick D M (1991) Heat capacities and entropies of sillimanite, fibrolite, andalusite, kyanite, and quartz and the Al_2SiO_5 phase diagram. Am Mineral 76: 1597–1613.

Hemingway B S, Robie R A, Evans H T, Kerrick D M (1991) Heat capacities and entropies of sillimanite, fibrolite, andalusite, kyanite, and quartz and the Al_2SiO_5 phase diagram. Am Mineral 76: 1597–1613.

Holland T J B, Carpenter M A (1986) Aluminium/silicon disordering and melting in sillimanite at high pressures. Nature 320: 151–153.

Hu X, Liu X, He Q, Wang H, Qin S, Ren L, Wu C M, Chang L (2011) Thermal expansion of andalusite and sillimanite at ambient pressure: a powder X-ray diffraction study up to 1000 °C. Mineral Mag 75: 363–374.

Ibberson R M (2009) Design and performance of the new supermirror guide on HRPD at ISIS. Nucl Instr Methods Phys Res A 600: 47–49.

Ibberson R M, David W I F, Knight K S (1992) The high resolution neutron powder diffractometer (HRPD) at ISIS – a user guide. RAL-92-031. Rutherford Appleton Laboratory, U.K.

Igami T, Kuribayashi T, Miyake A (2018) Determination of Al/Si order in sillimanite by high angular resolution electron channeling X-ray spectroscopy, and implications for determining peak temperatures of sillimanite. Am Mineral 103: 944–951.

Kaminski W (2004) *WinTensor* 1.1 (http://cad4.cpac.washington.edu/WinTensorhome/WinTensor.htm)

Kashcheev I D, Ust'yantsev V M, Sychev S N (2007) Kyanite concentrate of the Karabash deposit: phase transformations during heating. Refract Ind Ceram 48: 250–254.

Kerrick D M (1990) The Al_2SiO_5 polymorphs. Rev Mineral 22, Mineralogical Society of America, Chantilly, Virginia.

Koziol A M, Newton R C (1988) Redetermination of the anorthite breakdown reaction and improvement of the plagioclase–garnet–Al_2SiO_5–quartz geobarometer. Am Mineral 73: 216–223.

Larson A C, Von Dreele R B (1994) *General Structure Analysis System (GSAS)*, Los Alamos National Laboratory Report, LAUR 86-748.

Lafuente B, Downs R T, Yang H, Stone N (2015) The power of databases: the RRUFF project. In: *Highlights in Mineralogical Crystallography* (T Armbruster and R M Danisi, Eds), Berlin, Germany, W. De Gruyter, pp 1–30.

Lefebvre A, Paquet J (1983) Dissociation of *c* dislocation in sillimanite Al_2SiO_5. Bull Minéral 106: 287–292.

Liu X, He Q, Wang H, Fleet M, Hu X (2010) Thermal expansion of kyanite at ambient pressure: an X-ray powder diffraction study up to 1000 °C. Geosci Front 1: 91–97.

Liu X, Shieh S R, Fleet M E, Zhang L (2009) Compressibility of a natural kyanite to 17.5 GPa. Progr Nat Sci 19: 1281–1286.

Mantid (2013) Manipulation and Analysis Toolkit for Instrument Data; Mantid Project. http://dx.doi.org/10.5286/SOFTWARE/MANTID.

Mernagh T P, Liu L (1991) Raman spectra from the Al_2SiO_5 polymorphs at high pressure and room temperature, Phys Chem Mineral 18: 126–130

Neumann F (1925) Über die Stabilitätsverhältnisse der Modifikationen im polymorphen System Al_2SiO_5. Z Anorg Allgem Chem 145: 193–238.

Newton R C, Haselton H T (1981) Thermodynamics of the garnet–plagioclase–Al_2SiO_5–quartz geobarometer. In *Thermodynamics of minerals and melts,* Springer New York, pp. 131–147.

Oganov A R, Brodholt J B (2000) High-pressure phases in the Al_2SiO_5 system and the problem of aluminous phase in the Earth's lower mantle: *ab initio* calculations. Phys Chem Min 27: 430–439.

Page Y L, Saxe P (2002) Symmetry-general least-squares extraction of elastic data for strained materials from ab initio calculations of stress. Phys Rev B 65: 104104.

Pankratz L B, Kelley K K (1964) High temperature heat contents and entropies of andalusite, kyanite and sillimanite. U. S. Bur. Mines Rep. Invest. 6370.

Putz H, Brandenburg K (2006) *Diamond - Crystal and Molecular Structure Visualization.* Crystal Impact - GbR, Kreuzherrenstr. 102, 53227 Bonn, Germany. (http://www.crystalimpact.com/diamond)

Robie R A, Hemingway B S (1984) Entropies of kyanite, andalusite, and sillimanite: additional constraints on the pressure and temperature of the Al_2SiO_5 triple point. Am Mineral 69: 298–306.

Rossman G R, Grew E S, Dollase W A (1982) The colors of sillimanite. Am Mineral 67: 749–761.

Sainz M A, Serrano F J, Bastída J, Caballero A (1997) Microstructural evolution and growth of crystallite size of mullite during thermal transformation of kyanite. J Eur Ceram Soc 17: 1277–1284.

Salje E (1986) Heat capacities and entropies of andalusite and sillimanite: the influence of fibrolitization on the phase diagram of the Al_2SiO_5 polymorphs. Am Mineral 71: 1366–1371.

Schmidt M W, Poli S, Comodi P, Zanazzi P F (1997) High-pressure behavior of kyanite: decomposition of kyanite into stishovite and corundum. Am Mineral 82: 460–466.

Schneider H (1979) Thermal expansion of andalusite. J Am Ceram Soc 62, 307 (1 page article).

Skinner B J, Clark S P, Appleman D E (1961) Molar volumes and thermal expansions of andalusite, kyanite and sillimanite. Am J Sci 259: 651–668.

Toby B H (2001) EXPGUI, a graphical user interface for GSAS. J Appl Cryst 34: 210–213.

Tropper P, Hoinkes G (1996) Geothermobarometry of Al_2SiO_5-bearing metapelites in the western Austroalpine Ötztal-basement. Min Petrol 58: 145–170.

Vaughan M T, Weidner D J (1978) The relationship of elasticity and crystal structure in andalusite and sillimanite. Phys Chem Min 3: 133–144.

Winkler B, Hytha M, Warren M C, Milman V, Gale J D, Schreuer J (2001) Calculation of the elastic constants of the Al_2SiO_5 polymorphs andalusite, sillimanite and kyanite. Z Krist 216: 67–70.

Winter J K, Ghose S (1979) Thermal expansion and high-temperature crystal chemistry of the Al_2SiO_5 polymorphs. Am Mineral 64: 573–586.

Yang H, Downs R T, Finger L W, Hazen R M, Prewitt C T (1997a) Compressibility and crystal structure of kyanite, Al_2SiO_5, at high pressure. Am Mineral 82: 467–474.

Yang H, Hazen R M, Finger LW, Prewitt C T, Downs R T (1997b) Compressibility and crystal structure of sillimanite, Al_2SiO_5, at high pressure. Phys Chem Min 25: 39–47.

Yao H, Ouyang L, Ching W –Y (2007) Ab initio calculation of elastic constants of ceramic crystals. J Am Ceram Soc 90: 3194–3204.

Figure 1

Geometry of the silica-alumina chain structures found in each of the three Al_2SiO_5 polymorphs. Red spheres denote oxygen atoms, green spheres and surfaces are Al atoms and AlO_N polyhedra, and grey spheres and surfaces are Si atoms and SiO_4 tetrahedra. Drawn using Diamond (Putz & Branderburg, 2006).

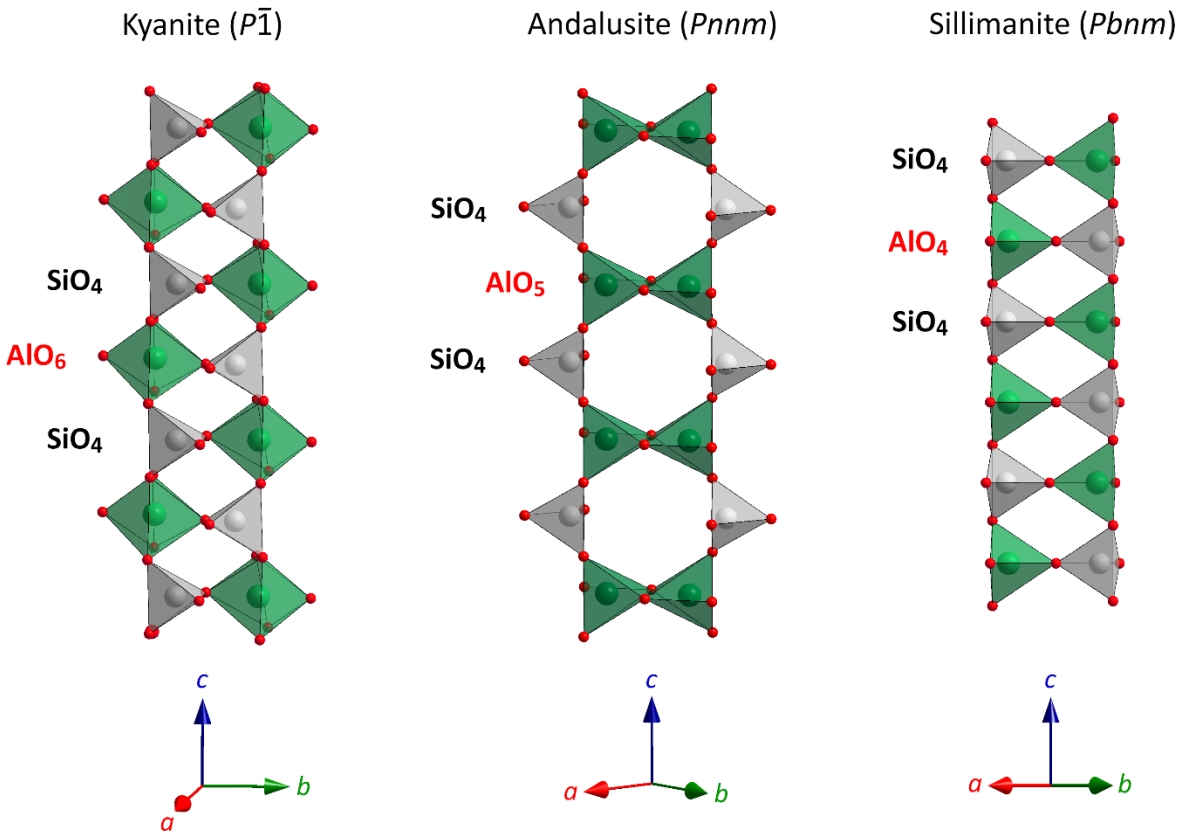

Figure 2

Stackplot of neutron powder diffraction patterns collected in the 'Risø' furnace on HRPD between 373 and 1573 K for each of the three Al_2SiO_5 polymorphs: (a) kyanite; (b) andalusite; (c) sillimanite. Diffraction indices of the strongest Bragg peaks in this range of d-spacings are indicated, in particular showing the presence of mullite in the highest-temperature data collected from kyanite (a).

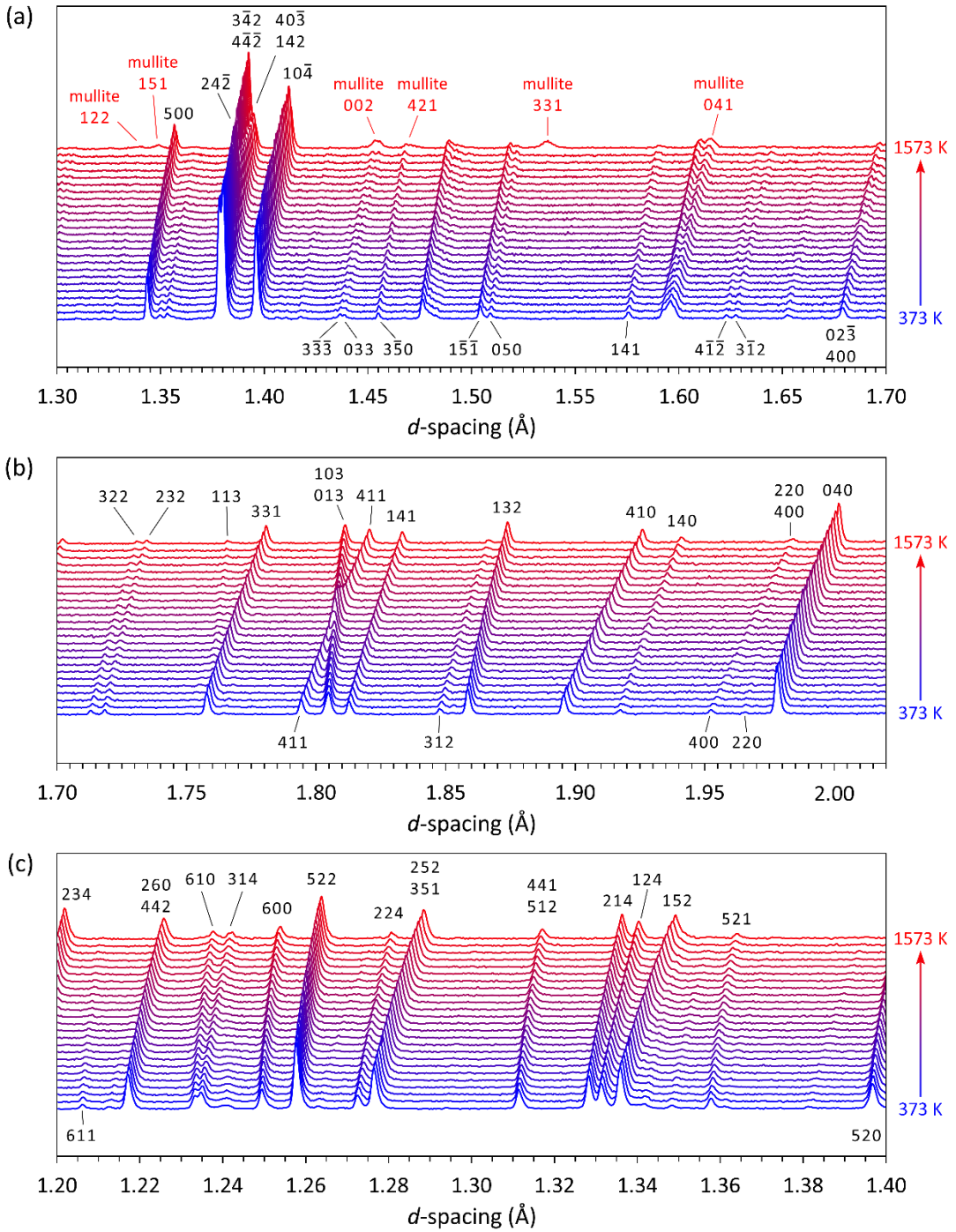

Figure 3

Examples of neutron powder diffraction data refinements carried out on each Al_2SiO_5 polymorph at 423 K. Red symbols are the measured data, green lines indicate the fitted models and purple lines underneath each diffraction pattern are difference profiles. Black vertical bars indicate the calculated positions of Bragg reflections. Insets report magnified views of the low d-spacing region of each diffraction pattern.

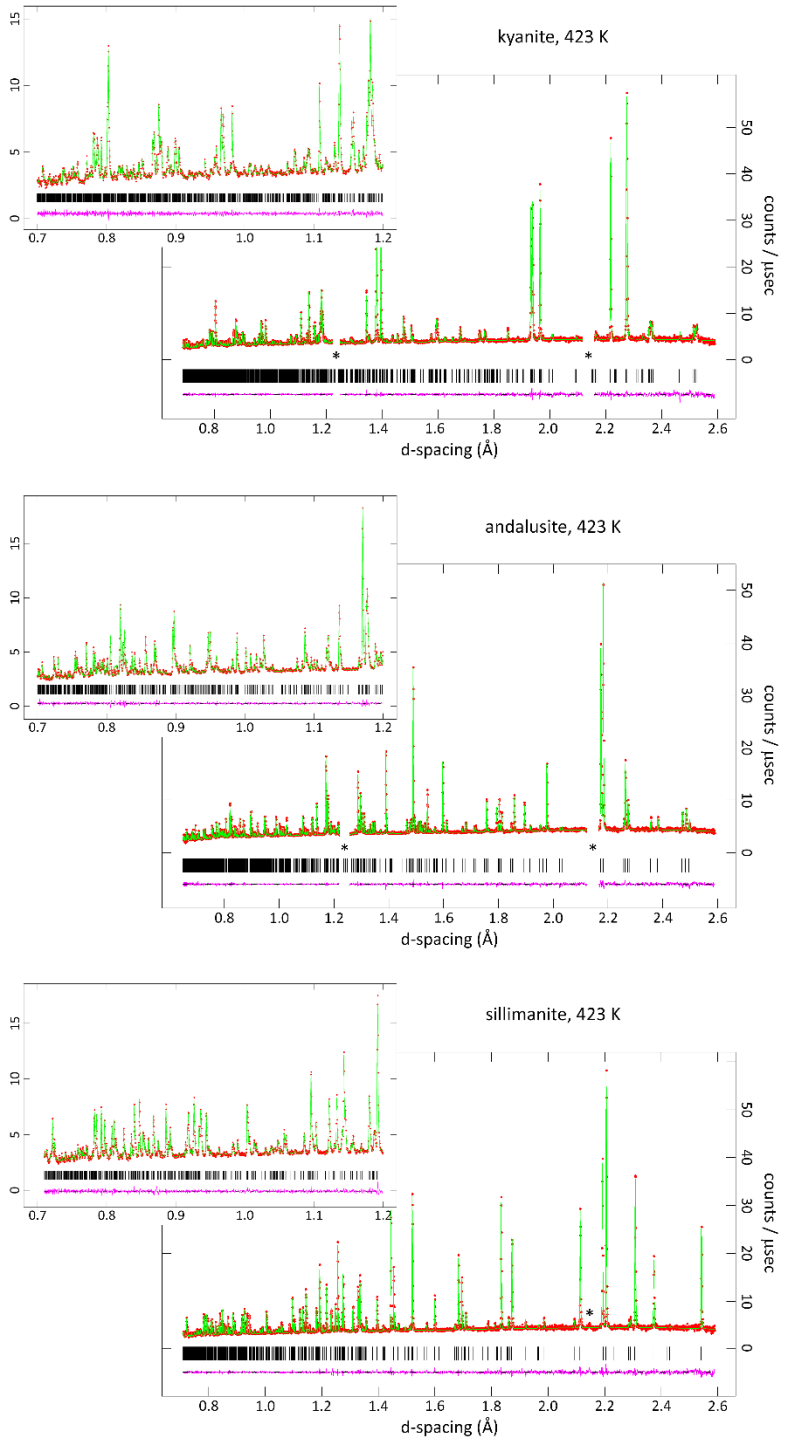

Figure 4

Lattice parameters of kyanite as a function of temperature from this work compared with literature values. The solid black lines represent the fit of a simplified model described in the text (Eq. 1).

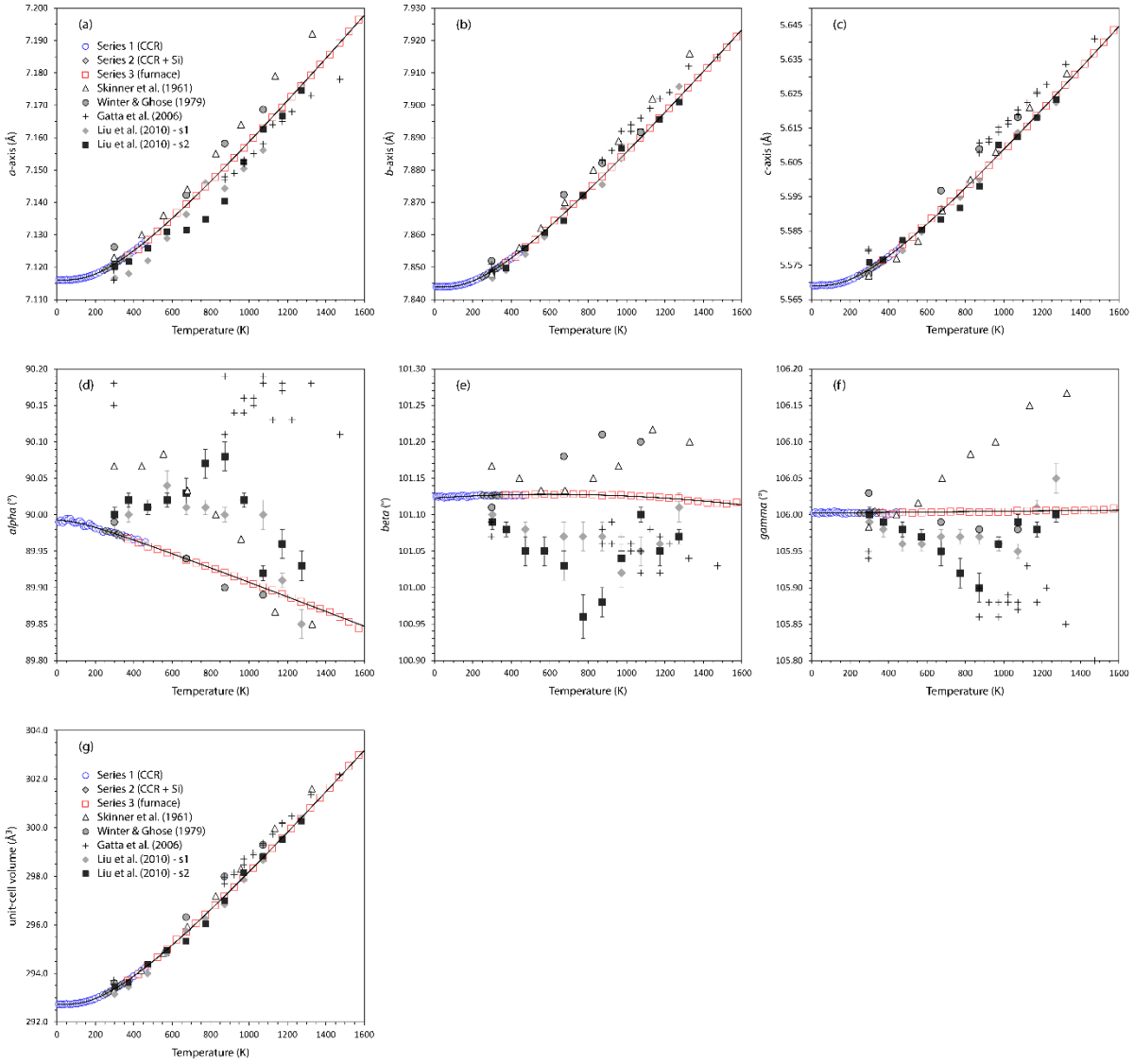

Figure 5

Lattice parameters and axial ratios of andalusite as a function of temperature from this work compared with literature values. The solid black lines represent the fit of a simplified model described in the text (Eq. 1).

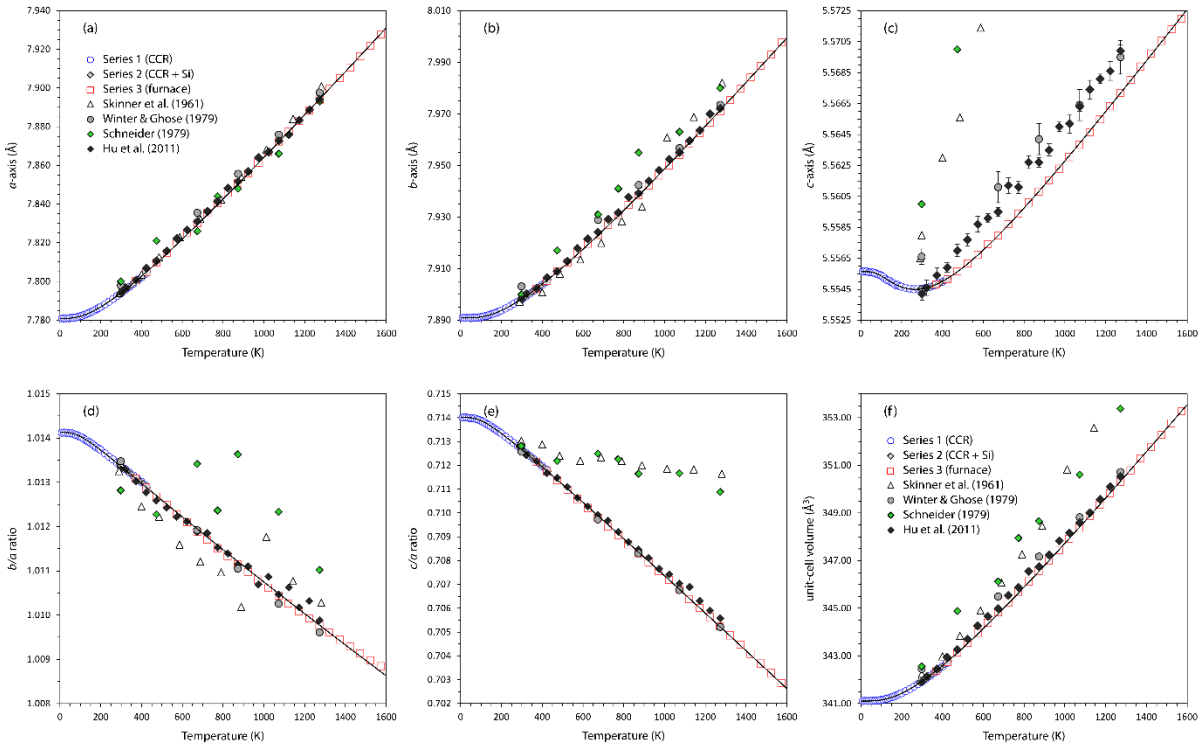

Figure 6

Lattice parameters and axial ratios of sillimanite as a function of temperature from this work compared with literature values. The solid black lines represent the fit of a simplified model described in the text (Eq. 1).

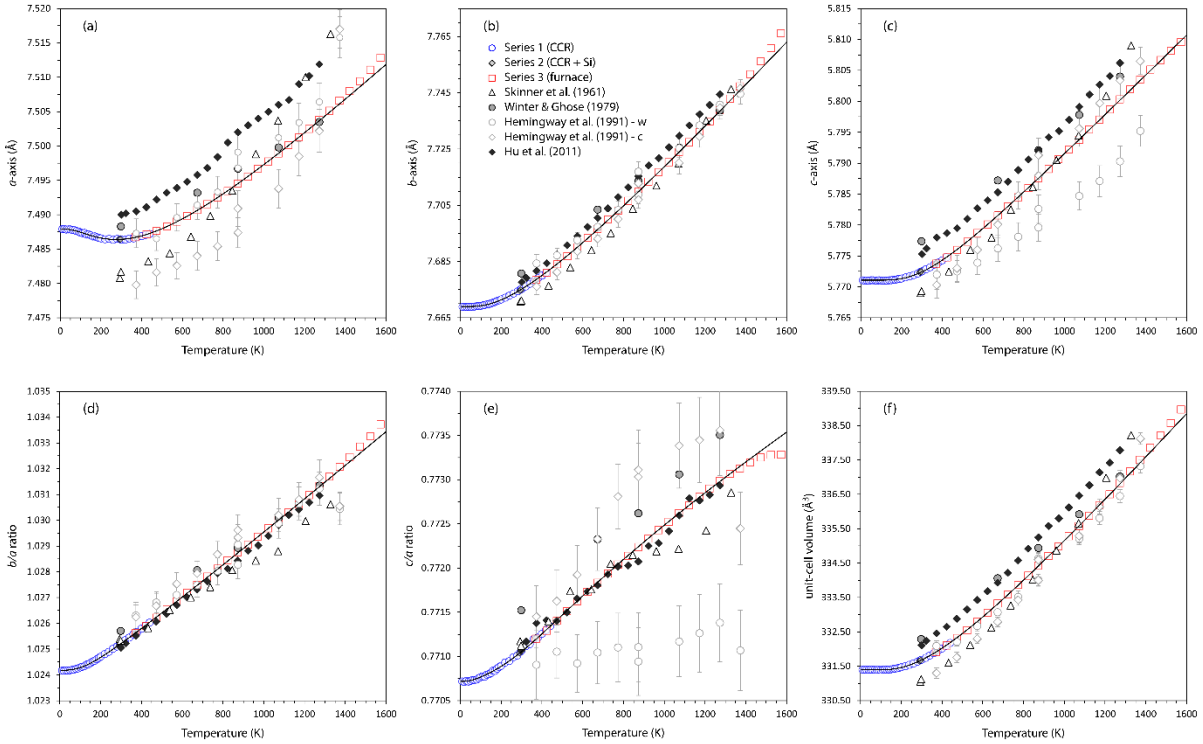

Figure 7

Coefficients, α_{ij}, of the thermal expansion tensor of kyanite derived both from the raw experimental data (symbols) and from the model fits shown in Figure 4 (lines).

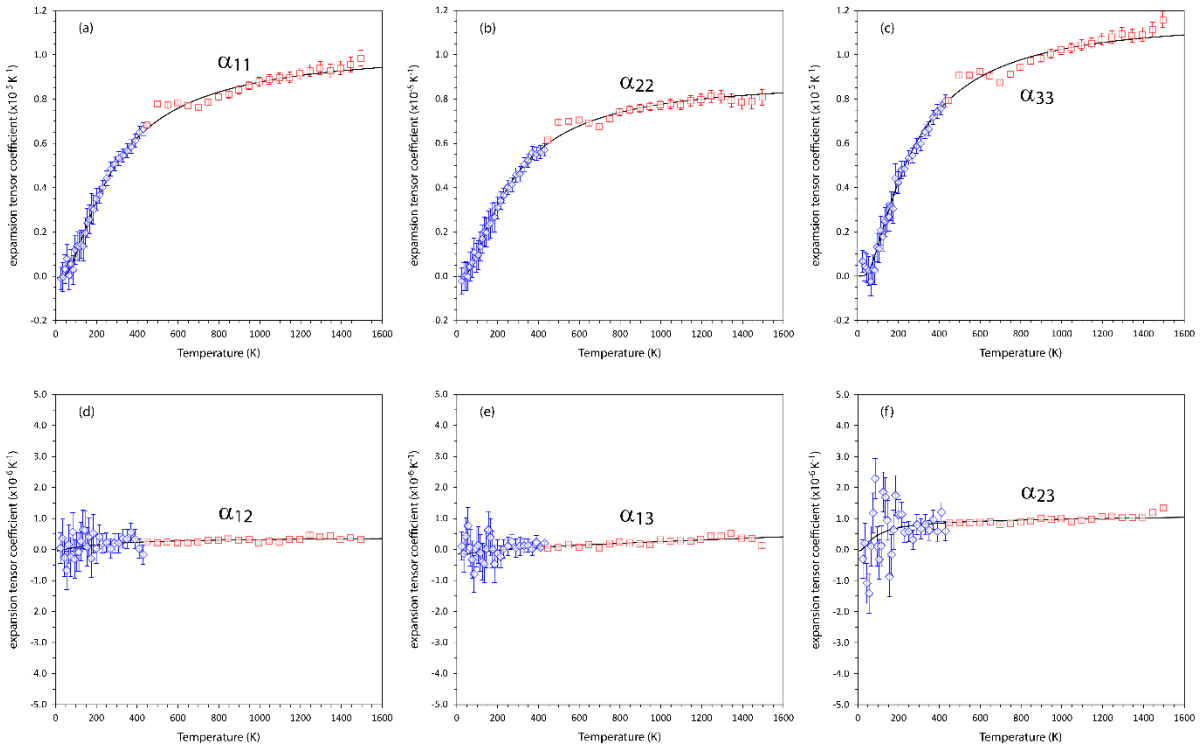

Figure 8

Linear expansion coefficients (α_a, α_b, α_c) and volume thermal expansion coefficient (α_V) of andalusite derived both from the raw experimental data (symbols) and from the model fits shown in Figure 5 (lines).

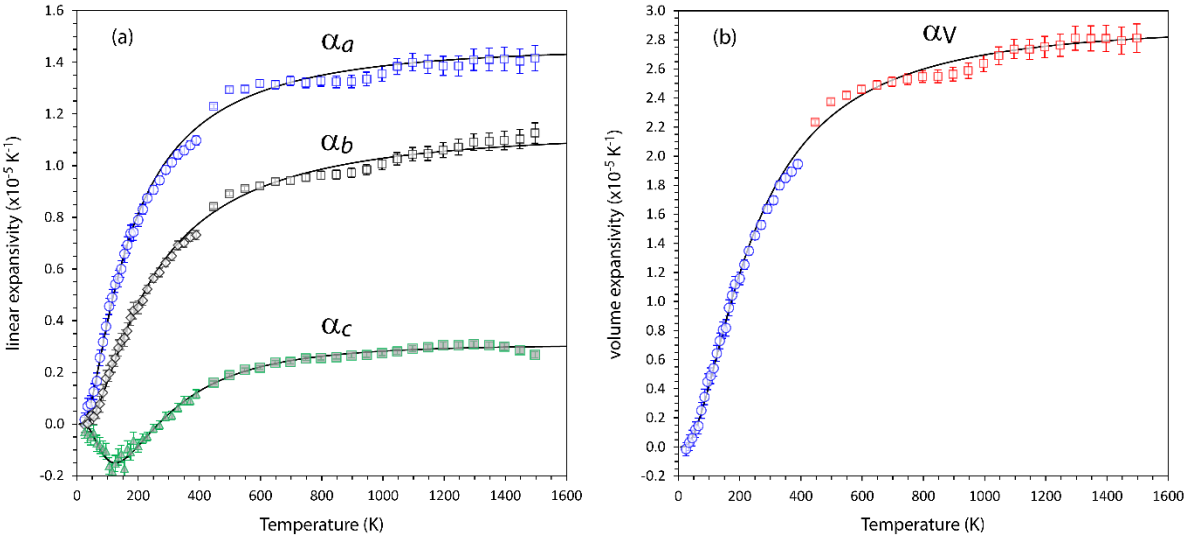

Figure 9

Linear expansion coefficients (α_a, α_b, α_c) and volume thermal expansion coefficient (α_V) of sillimanite derived both from the raw experimental data (symbols) and from the model fits shown in Figure 6 (lines).

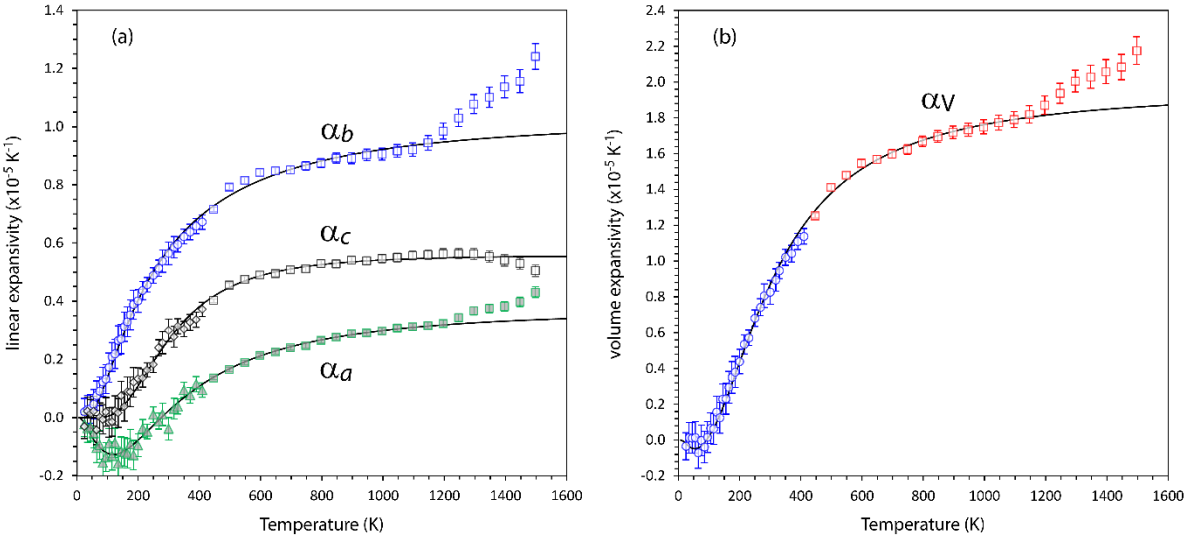

Figure 10

Comparison of the model values of α_V for each of the three Al_2SiO_5 polymorphs.

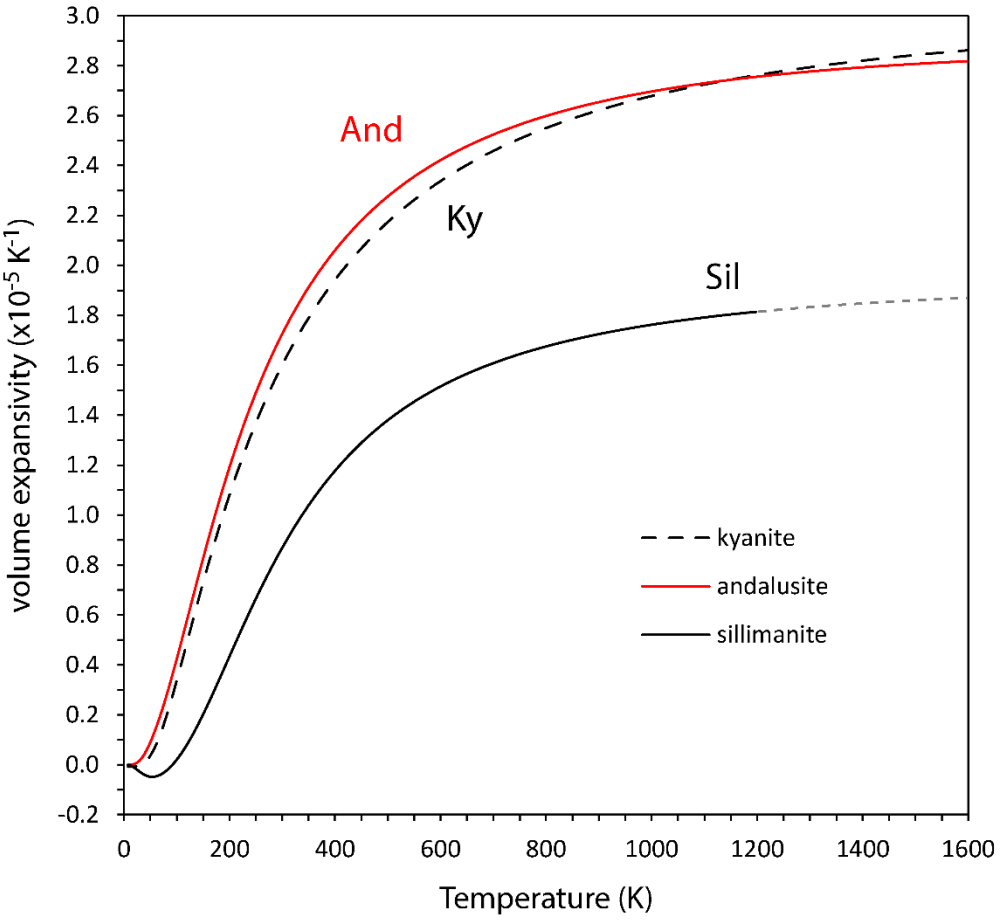

Figure 11

Comparison of the linear expansion coefficients of andalusite with the principal values of kyanite's thermal expansion tensor (left); comparison of the linear expansion coefficients of andalusite and sillimanite (right). The orientation of α_1, α_2 and α_3 with respect to kyanite's unit cell edges is shown in Figure 12.

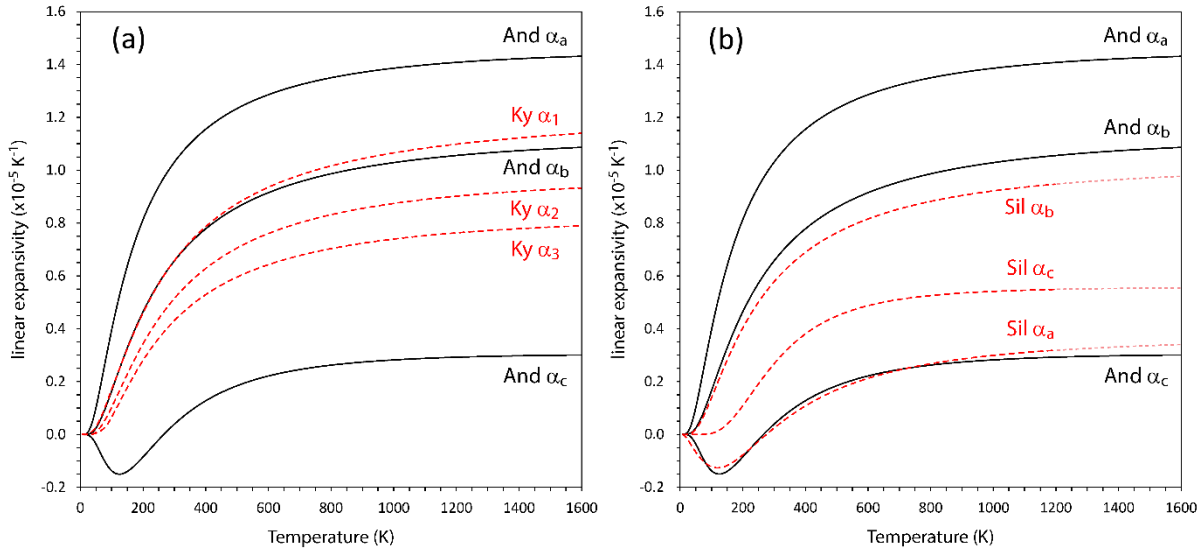

Figure 12

Representation surfaces of the kyanite thermal expansion tensor at 1500 K, drawn using WinTensor (Kaminski, 2004) are shown in the centre, with arrows to indicate the orientation of both the principal directions and the unit-cell edges. Sections of the tensor surface on *a**, *b* and *c* as a function of temperature are shown on the left. Polyhedral depictions of kyanite's crystal structure, similarly projected on *a**, *b* and *c* are shown on the right.

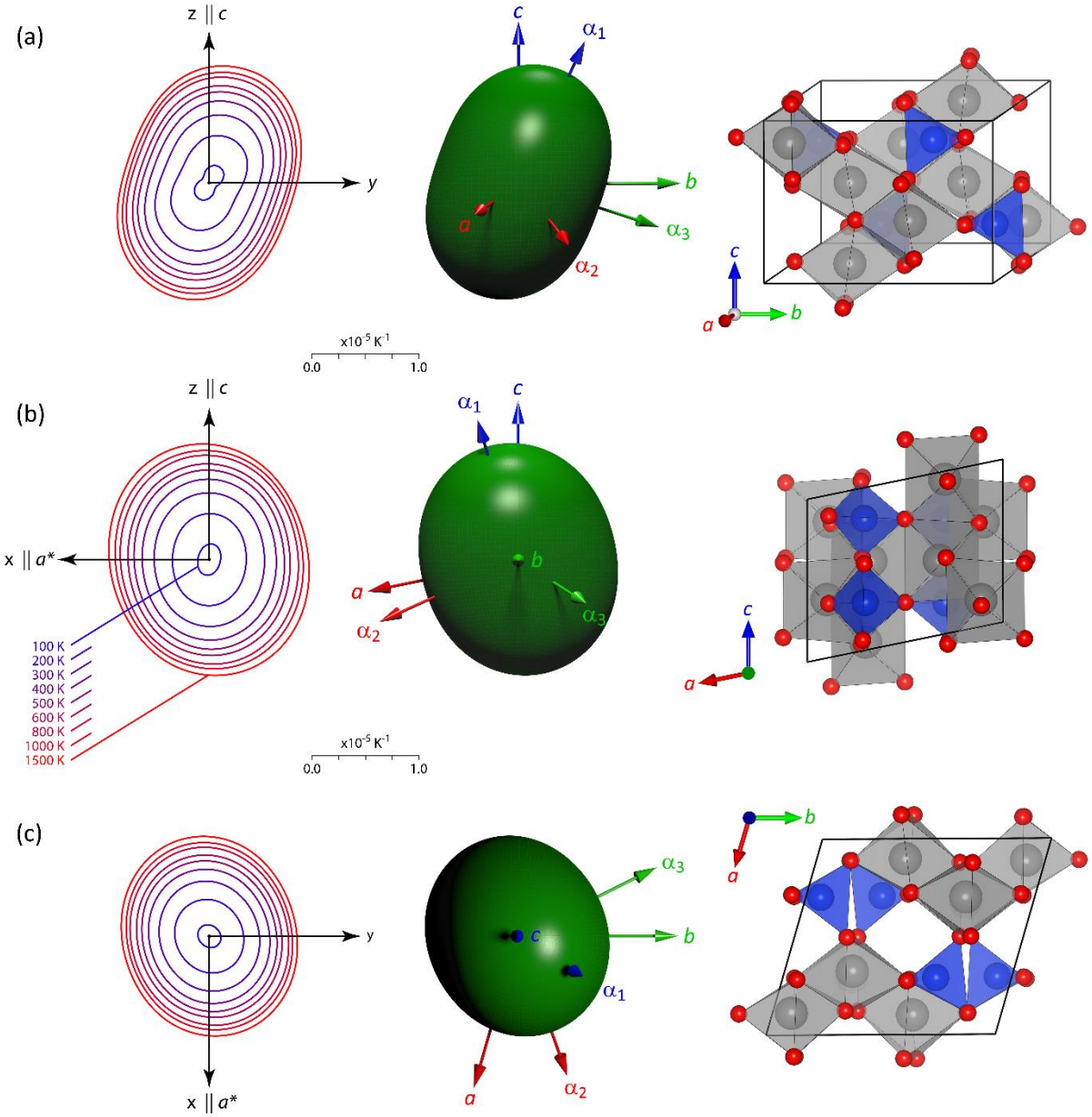

Figure 13

Gatta et al. (2006) reported their kyanite thermal expansion tensors as strain ellipsoids (their Figure 4) superimposed over two projections of the structure (bottom). In order to provide a more exact comparison, I show my results in the same manner (top).

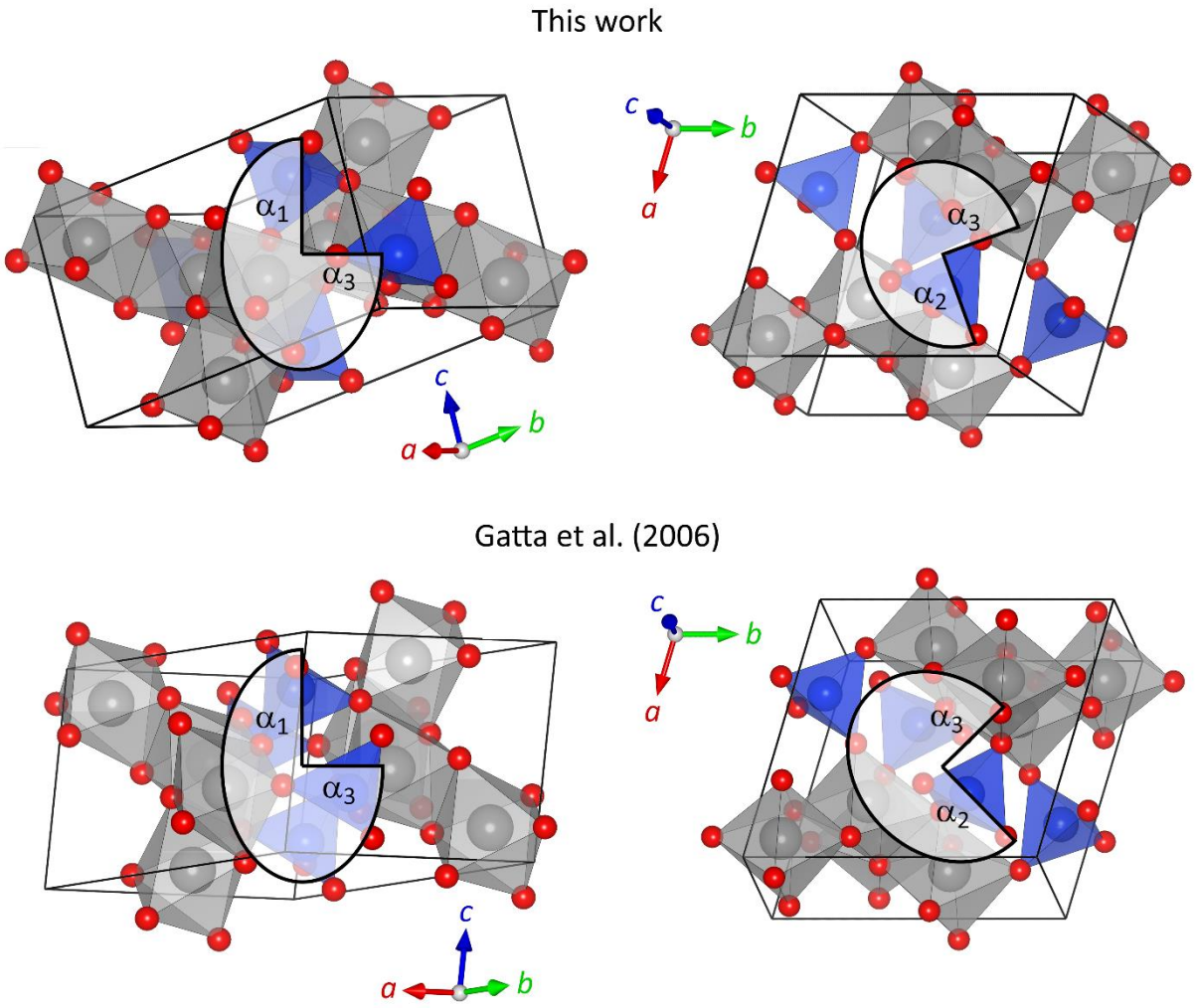

Figure 14

Expanded view of the *c*-axis length in andalusite and the *a*-axis length in sillimanite at low temperatures, emphasising both the negative linear expansion and the general similarities between the two.

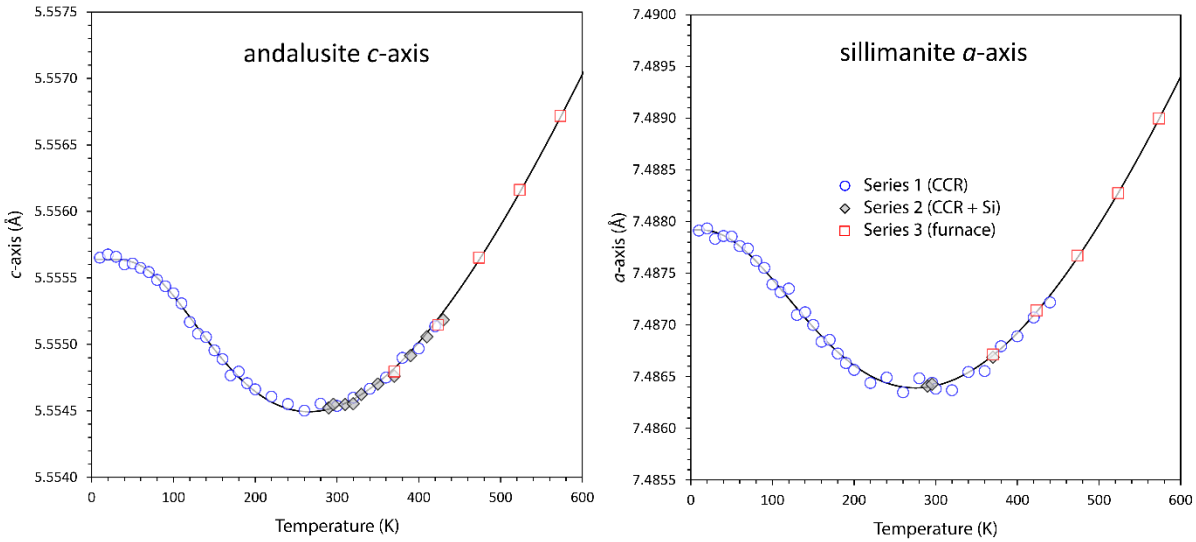

Figure 15

View of the sillimanite structure along the *c*-axis. Bold green and grey tetrahedra denote the chains of AlO_4 and SiO_4 (as seen in Figure 1) viewed 'end-on'; the faint green octahedra denote the chains of edge-sharing AlO_6.

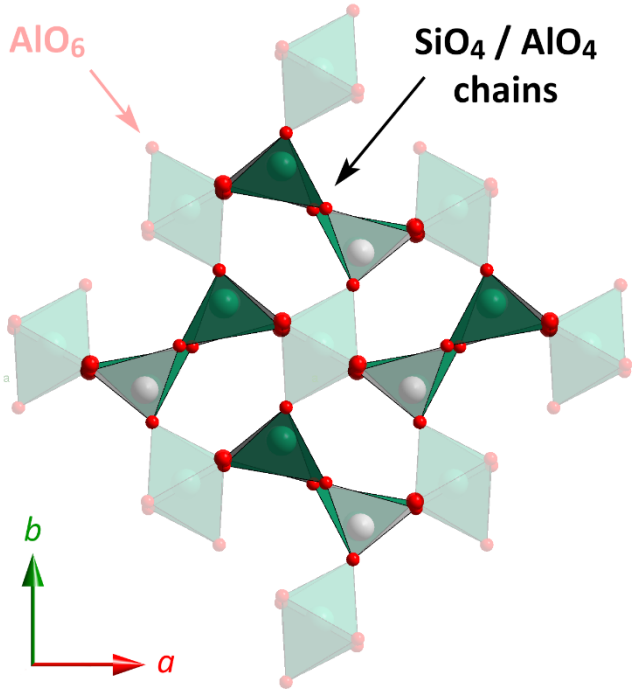

Tables

Table 1

Composition (wt. %) of the materials used in this study, determined by electron microprobe.

	Kyanite	Andalusite	Sillimanite
Al_2O_3	62.4(3)	62.0(2)	61.7(2)
SiO_2	37.8(8)	37.6(2)	37.5(4)
FeO	0.17(2)	0.34(6)	0.99(2)
MgO	0.03(1)	0.08(2)	0.002(2)
Cr_2O_3	0.01(1)	0.002(3)	0.001(1)
MnO	0.002(3)	0.002(3)	0.001(2)
TiO_2	0.01(1)	0.03(1)	0.01(1)
Na_2O	0.01(1)	0.01(1)	0.01(1)
K_2O	0.01(1)	0.006(4)	0.01(1)
CaO	0.006(4)	0.003(3)	0.005(3)
Total	100.4(7)	100.0(3)	100.2(5)

Table 2

Parameters obtained from fitting Eq. 1 to the unit-cell parameters of kyanite in the range 10 – 1573 K. Units for X_0 and the residuals are Å, degrees or Å^3 as appropriate. The term S is given by Eqs. 2–6.

	a-axis	*b*-axis	*c*-axis	Volume
	S = A	S = A	S = A	S = A
X_0	7.11610(3)	7.84390(3)	5.56906(6)	292.734(6)
a	7.35(2)x10^{-5}	7.08(2)x10^{-5}	6.70(2)x10^{-5}	9.37(2)x10^{-3}
b	−78.9(4)	−76.9(4)	−75.7(7)	−78.5(5)
R^2	99.9969 %	99.9960 %	99.9914 %	99.9961 %
Max residual	0.00062	0.00066	0.00065	0.064
	α	β	γ	
	S = A	quadratic	linear	
X_0	89.9920(8)	101.1228(3)	106.0022(2)	
a	−1.04(1)x10^{-4}	1.7(1)x10^{-5}	2.7(2)x10^{-6}	
b	−29(3)	−1.41(7)x10^{-8}	–	
R^2	99.8905 %	89.2737 %	66.5304 %	
Max residual	0.0055	0.0027	0.0026	

Table 3

Parameters obtained from fitting Eq. 1 to the unit-cell parameters of andalusite in the range 10 – 1573 K. Units for X_0 and the residuals are Å, degrees or Å^3 as appropriate. The term S is given by Eqs. 2–5.

	a-axis S = A	*b*-axis S = A	*c*-axis S = A + B	Volume S = A
X_0	7.78093(7)	7.89085(4)	5.55564(2)	341.102(6)
a	$1.195(3)\times10^{-4}$	$9.39(2)\times10^{-5}$	$-5.6(4)\times10^{-5}$	$1.079(3)\times10^{-2}$
b	−52.4(4)	−70.2(4)	−62(3)	−70.7(5)
c	–	–	$7.2(4)\times10^{-5}$	–
d	–	–	−501(7)	–
R^2	99.9922 %	99.9954 %	99.9912 %	99.9932 %
Max residual	0.00090	0.00055	0.00014	0.060

Table 4

Parameters obtained from fitting Eq. 1 to the unit-cell parameters of sillimanite in the range 10 – 1177 K. Units for X_0 and the residuals are Å, degrees or Å^3 as appropriate. The term S is given by Eqs. 2–5.

	a-axis S = A + B	*b*-axis S = A	*c*-axis S = C	Volume S = B
X_0	7.48792(2)	7.66900(2)	5.77108(1)	331.392(2)
a	$-1.7(1)\times10^{-5}$	$8.20(3)\times10^{-5}$	$3.252(7)\times10^{-5}$	$6.70(2)\times10^{-3}$
b	−27(3)	−72.1(4)	389(2)	−575(2)
c	$4.5(1)\times10^{-5}$	–	–	–
d	−649(12)	–	–	–
R^2	99.9944 %	99.9890 %	99.9957 %	99.9955 %
Max residual	0.00010	0.00033	0.00012	0.019

Table 5

Comparison of molar volumes, V, and differences in molar volume, ΔV, between each polymorph (all in units of $cm^3\ mol^{-1}$).

	This work 295.65 K	Skinner et al. (1961) 298.15 K	Winter & Ghose (1979) 298.15 K
V_{Ky}	44.1611(3)	44.116(21)	44.221(14)
V_{And}	51.4750(2)	51.550(11)	51.579(9)
V_{Sil}	49.9345(3)	49.918(15)	50.049(7)
ΔV (And-Ky)	7.3139(4)	7.434(24)	7.358(17)
ΔV (Sil-Ky)	5.7734(4)	5.802(26)	5.828(16)
ΔV (And-Sil)	1.5405(4)	1.632(19)	1.530(11)

Thermal expansion of the Al_2SiO_5 polymorphs, kyanite, andalusite and sillimanite, between 10 and 1573 K determined using time-of-flight neutron powder diffraction.

A. Dominic Fortes,[1,2,†]

[1]ISIS Facility, STFC Rutherford Appleton Laboratory, Harwell Science and Innovation Campus, Chilton, Didcot, Oxfordshire, OX11 0QX, U.K.
[2]Department of Earth Sciences, University College London, Gower Street, London WC1E 6BT, U.K.

Corresponding author email dominic.fortes@stfc.ac.uk

Contents

Table S1:

Spherical harmonic texture coefficients (C_L^{mn}) and the texture index (J) for the three Al_2SiO_5 polymorphs in the slab-geometry sample holders at 300 K. Models with cylindrical symmetry were fitted to 6th order for kyanite and andalusite, and to 8th order for sillimanite. Further quantitative analyses of the preferred orientation, derived from these values, are given in Table S2 and in Figure S2.

kyanite				andalusite		sillimanite	
C_L^{mn}		C_L^{mn}		C_L^{mn}		C_L^{mn}	
$20\bar{2}$	−0.028(11)	$60\bar{6}$	−0.065(16)	200	−0.287(5)	200	−0.959(5)
$20\bar{1}$	0.137(8)	$60\bar{5}$	0.035(16)	202	0.137(5)	202	−1.962(6)
200	−0.979(6)	$60\bar{4}$	−0.013(15)	400	−0.005(6)	400	0.459(6)
201	0.332(7)	$60\bar{3}$	−0.007(16)	402	0.007(7)	402	0.763(7)
202	0.408(8)	$60\bar{2}$	−0.055(17)	404	0.018(8)	404	1.168(8)
$40\bar{4}$	0.096(16)	$60\bar{1}$	0.017(13)	600	−0.084(7)	600	−0.201(6)
$40\bar{3}$	0.015(14)	600	−0.099(14)	602	−0.045(9)	602	−0.222(9)
$40\bar{2}$	0.052(14)	601	0.094(14)	604	0.016(8)	604	−0.304(9)
$40\bar{1}$	−0.129(11)	602	0.046(12)	606	0.038(9)	606	−0.458(10)
400	0.387(9)	603	−0.030(12)	–	–	800	0.012(9)
401	−0.229(11)	604	0.028(11)	–	–	802	0.124(12)
402	−0.092(10)	605	0.002(12)	–	–	804	0.047(10)
403	0.111(8)	606	0.089(10)	–	–	806	0.080(9)
404	0.202(9)	–	–	–	–	808	0.087(12)
		J	1.286(2)	J	1.0211(5)	J	2.223(4)

Table S2:

Maximum and minimum pole-figure values, P_{max} and P_{min}, in multiples of a random distribution (MRD), along three directions, *001*, *010* and *001*, in each of the three Al_2SiO_5 polymorphs. Significant preferred orientation is present in both the slab- and cylindrical-geometry sample holders used in the CCR and furnace, respectively. However, the texture is clearly more severe in the slab-geometry holders and for sillimanite in particular. Illustrations of the inverse pole figures along *001* are shown in Figure S2.

	Slab-geometry can, 300 K			**Cylindrical can, 423 K**		
kyanite	*1 0 0*	*0 1 0*	*0 0 1*	*1 0 0*	*0 1 0*	*0 0 1*
P_{min}	0.71	0.87	0.31	0.68	0.95	0.81
P_{max}	2.51	1.53	1.66	1.24	1.03	1.40
andalusite	*1 0 0*	*0 1 0*	*0 0 1*	*1 0 0*	*0 1 0*	*0 0 1*
P_{min}	0.86	0.99	0.62	0.81	0.98	0.93
P_{max}	1.29	1.05	1.17	1.06	1.02	1.14
sillimanite	*1 0 0*	*0 1 0*	*0 0 1*	*1 0 0*	*0 1 0*	*0 0 1*
P_{min}	0.19	0.31	0.31	0.78	0.45	0.87
P_{max}	1.89	5.46	1.74	1.46	1.41	1.25

Table S3:

Refined lattice parameters of kyanite

T (K)	*a* (Å)	*b* (Å)	*c* (Å)	α (°)	β (°)	γ (°)	V (Å^3)
Kyanite series one (Ky, Al slab-can, CCR)							
10.0	7.116084(26)	7.843953(19)	5.569067(29)	89.9903(10)	101.1250(5)	106.0022(5)	292.731(2)
20.0	7.116138(31)	7.843987(22)	5.569111(35)	89.9921(12)	101.1244(5)	106.0037(6)	292.735(2)
30.0	7.116073(31)	7.843911(22)	5.569106(35)	89.9893(12)	101.1253(5)	106.0021(6)	292.732(2)
40.0	7.116064(32)	7.843904(23)	5.569178(36)	89.9917(12)	101.1249(6)	106.0019(6)	292.735(2)
50.0	7.116190(28)	7.843971(21)	5.569215(34)	89.9947(11)	101.1233(5)	106.0040(5)	292.742(2)
60.0	7.116111(32)	7.843956(23)	5.569164(36)	89.9933(13)	101.1239(6)	106.0023(6)	292.738(2)
70.0	7.116133(32)	7.843978(22)	5.569181(36)	89.9944(12)	101.1235(6)	106.0025(6)	292.740(2)
80.0	7.116149(32)	7.844010(22)	5.569143(36)	89.9907(12)	101.1248(5)	106.0021(6)	292.740(2)
90.0	7.116249(31)	7.844126(22)	5.569213(36)	89.9891(12)	101.1250(5)	106.0038(6)	292.750(2)
100.0	7.116292(31)	7.844168(22)	5.569263(36)	89.9889(12)	101.1247(5)	106.0028(6)	292.758(2)
110.0	7.116392(31)	7.844250(22)	5.569356(35)	89.9902(12)	101.1248(5)	106.0032(6)	292.769(2)
120.0	7.116562(29)	7.844386(22)	5.569428(35)	89.9915(12)	101.1236(5)	106.0048(5)	292.783(2)
130.0	7.116597(31)	7.844497(22)	5.569617(36)	89.9883(12)	101.1253(5)	106.0032(6)	292.800(2)
140.0	7.116741(30)	7.844614(22)	5.569655(36)	89.9842(11)	101.1260(5)	106.0036(6)	292.813(2)
150.0	7.116866(30)	7.844748(22)	5.569828(35)	89.9842(11)	101.1263(5)	106.0028(6)	292.833(2)
160.0	7.117007(32)	7.844874(23)	5.570017(37)	89.9850(12)	101.1256(5)	106.0018(6)	292.855(2)
170.0	7.117207(32)	7.845142(23)	5.570104(37)	89.9877(12)	101.1240(6)	106.0028(6)	292.878(2)
180.0	7.117385(32)	7.845263(23)	5.570358(37)	89.9852(12)	101.1253(5)	106.0015(6)	292.904(2)
190.0	7.117664(31)	7.845538(23)	5.570544(36)	89.9833(11)	101.1254(5)	106.0032(6)	292.933(2)
200.0	7.117898(31)	7.845712(23)	5.570842(37)	89.9815(11)	101.1261(5)	106.0025(6)	292.966(2)

220.0	7.118400(31)	7.846240(23)	5.571300(37)	89.9801(11)	101.1261(5)	106.0026(6)	293.031(2)
240.0	7.119025(30)	7.846804(22)	5.571892(37)	89.9764(10)	101.1274(5)	106.0027(6)	293.108(2)
260.0	7.119623(30)	7.847393(23)	5.572402(37)	89.9779(10)	101.1265(5)	106.0022(6)	293.183(2)
280.0	7.120286(30)	7.848090(23)	5.573084(36)	89.9764(10)	101.1260(5)	106.0024(6)	293.273(2)
300.0	7.121060(30)	7.848774(23)	5.573707(37)	89.9750(10)	101.1261(5)	106.0034(6)	293.362(2)
320.0	7.121807(29)	7.849504(22)	5.574404(36)	89.9715(9)	101.1269(5)	106.0030(6)	293.458(2)
340.0	7.122552(29)	7.850245(23)	5.575085(34)	89.9723(9)	101.1258(4)	106.0025(6)	293.554(2)
360.0	7.123392(27)	7.851077(22)	5.575889(33)	89.9699(8)	101.1260(4)	106.0027(5)	293.662(2)
380.0	7.124211(28)	7.851907(22)	5.576652(34)	89.9690(8)	101.1264(4)	106.0016(6)	293.768(2)
400.0	7.125070(28)	7.852738(22)	5.577481(35)	89.9659(7)	101.1264(4)	106.0006(5)	293.881(2)
420.0	7.125993(28)	7.853620(23)	5.578293(34)	89.9660(8)	101.1257(4)	106.0018(6)	293.994(2)
440.0	7.126985(27)	7.854573(23)	5.579154(35)	89.9613(7)	101.1267(4)	106.0036(5)	294.113(2)
460.0	7.127896(26)	7.855501(22)	5.580116(34)	89.9624(7)	101.1260(4)	106.0031(5)	294.238(2)

Kyanite series two (Ky + NIST silicon, Al slab can, CCR)

250.0	7.119142(30)	7.846975(23)	5.572007(37)	89.9779(10)	101.1268(5)	106.0020(6)	293.127(2)
270.0	7.119881(29)	7.847659(23)	5.572610(37)	89.9768(10)	101.1263(5)	106.0027(6)	293.214(2)
295.65	7.120718(22)	7.848418(18)	5.573512(30)	89.9754(7)	101.1260(4)	106.0031(4)	293.325(2)
310.0	7.121392(29)	7.849106(23)	5.573998(38)	89.9728(9)	101.1267(5)	106.0034(6)	293.403(2)
320.0	7.121820(29)	7.849499(23)	5.574399(38)	89.9743(9)	101.1260(5)	106.0039(6)	293.456(2)
330.0	7.122229(27)	7.849836(23)	5.574841(38)	89.9722(9)	101.1255(5)	106.0051(5)	293.508(2)
350.0	7.122929(27)	7.850599(22)	5.575518(38)	89.9684(8)	101.1269(4)	106.0037(5)	293.603(2)
370.0	7.123765(27)	7.851445(23)	5.576268(38)	89.9686(8)	101.1263(4)	106.0036(5)	293.710(2)

Kyanite series three (Ky, vanadium cylinder, furnace)

369.9	7.123556(21)	7.851301(20)	5.576560(13)	89.9669(4)	101.1269(2)	106.0022(5)	293.713(1)
423.5	7.125549(26)	7.85322(25)	5.578373(17)	89.9619(5)	101.1274(3)	106.0017(5)	293.964(1)
473.5	7.128533(26)	7.856175(26)	5.581077(17)	89.9565(4)	101.1272(3)	106.0033(5)	294.340(1)

523.4	7.131042(27)	7.858604(26)	5.583348(17)	89.9525(4)	101.1278(3)	106.0026(5)	294.656(1)
573.4	7.133886(27)	7.861364(27)	5.585956(18)	89.9478(4)	101.1285(3)	106.0031(5)	295.015(1)
623.4	7.136786(26)	7.864318(25)	5.588686(17)	89.9431(4)	101.1271(3)	106.0039(4)	295.392(1)
673.3	7.139452(27)	7.866855(28)	5.591093(18)	89.9384(4)	101.1290(3)	106.0039(4)	295.724(1)
723.1	7.142099(26)	7.869458(27)	5.593510(18)	89.9340(4)	101.1280(3)	106.0043(4)	296.061(1)
772.9	7.144963(28)	7.872196(29)	5.595995(19)	89.9300(4)	101.1283(3)	106.0047(4)	296.415(1)
822.7	7.147808(27)	7.875098(28)	5.598724(19)	89.9254(4)	101.1279(3)	106.0036(4)	296.790(1)
872.5	7.150701(26)	7.878046(28)	5.601404(19)	89.9207(3)	101.1263(3)	106.0040(4)	297.167(1)
922.2	7.153707(28)	7.880871(28)	5.604127(19)	89.9157(4)	101.1275(3)	106.0035(4)	297.544(1)
972.1	7.156788(27)	7.88393(29)	5.606965(19)	89.9099(4)	101.1273(3)	106.0041(4)	297.939(1)
1021.9	7.159904(28)	7.886961(30)	5.609818(20)	89.9053(4)	101.1261(4)	106.0041(4)	298.338(1)
1071.5	7.163029(27)	7.889943(28)	5.612685(19)	89.9009(3)	101.1247(3)	106.0057(4)	298.734(1)
1121.2	7.166198(28)	7.892989(30)	5.615574(20)	89.8965(4)	101.1252(4)	106.0052(4)	299.137(1)
1170.6	7.169382(28)	7.896014(29)	5.618530(20)	89.8910(4)	101.1239(4)	106.0061(4)	299.544(1)
1220.4	7.172557(29)	7.899139(31)	5.621467(20)	89.8863(4)	101.1229(4)	106.0060(4)	299.955(1)
1270.5	7.175923(30)	7.902312(31)	5.624545(21)	89.8807(4)	101.1224(4)	106.0062(4)	300.382(1)
1320.3	7.179230(28)	7.905434(30)	5.627617(20)	89.8754(4)	101.1192(4)	106.0048(3)	300.811(1)
1370.0	7.182533(30)	7.908581(31)	5.630675(21)	89.8712(4)	101.1183(4)	106.0057(4)	301.234(1)
1420.1	7.185724(31)	7.911547(31)	5.633689(21)	89.8662(4)	101.1164(4)	106.0056(4)	301.646(1)
1470.2	7.189260(31)	7.914693(32)	5.636817(21)	89.8599(4)	101.1156(4)	106.0066(4)	302.083(1)
1520.6	7.192787(32)	7.917881(33)	5.640128(22)	89.8531(4)	101.1152(5)	106.0072(4)	302.532(1)
1571.3	7.196441(44)	7.921169(46)	5.643553(33)	89.8444(6)	101.1172(6)	106.0087(5)	302.993(1)

Table S4:

Refined lattice parameters of andalusite

T (K)	*a* (Å)	*b* (Å)	*c* (Å)	V (Å^3)
Andalusite series one (And, Al slab-can, CCR)				
10.0	7.780992(15)	7.890867(17)	5.555652(13)	341.110(1)
20.0	7.780952(19)	7.890858(22)	5.555676(16)	341.110(1)
30.0	7.780970(19)	7.890850(22)	5.555659(16)	341.109(1)
40.0	7.781033(18)	7.890860(21)	5.555602(16)	341.109(1)
50.0	7.781111(19)	7.890862(22)	5.555609(16)	341.113(1)
60.0	7.781152(19)	7.890928(22)	5.555576(16)	341.115(1)
70.0	7.781327(19)	7.890927(21)	5.555544(16)	341.121(1)
80.0	7.781500(19)	7.890987(22)	5.555485(16)	341.127(1)
90.0	7.781751(19)	7.891110(22)	5.555438(16)	341.141(1)
100.0	7.782070(19)	7.891215(22)	5.555384(16)	341.156(1)
110.0	7.782383(19)	7.891404(22)	5.555309(16)	341.173(1)
120.0	7.782815(19)	7.891574(22)	5.555168(16)	341.191(1)
130.0	7.783214(20)	7.891766(23)	5.555081(17)	341.211(1)
140.0	7.783645(20)	7.892009(23)	5.555055(17)	341.239(1)
150.0	7.784130(20)	7.892271(22)	5.554955(16)	341.266(1)
160.0	7.784615(19)	7.892523(22)	5.554889(16)	341.294(1)
170.0	7.785182(19)	7.892797(22)	5.554768(17)	341.323(1)
180.0	7.785748(20)	7.893123(22)	5.554795(17)	341.364(1)
190.0	7.786339(19)	7.893499(22)	5.554708(17)	341.401(1)
200.0	7.786918(19)	7.893836(22)	5.554662(17)	341.438(1)
220.0	7.788208(20)	7.894550(23)	5.554608(17)	341.522(1)
240.0	7.789575(20)	7.895387(23)	5.554551(17)	341.614(1)
260.0	7.791002(19)	7.896307(23)	5.554503(17)	341.714(1)
280.0	7.792445(19)	7.897223(22)	5.554554(17)	341.820(1)
300.0	7.793985(20)	7.898168(24)	5.554538(18)	341.927(1)
320.0	7.795602(20)	7.899266(23)	5.554599(18)	342.050(1)
340.0	7.797181(20)	7.900302(23)	5.554667(18)	342.168(1)
360.0	7.798867(20)	7.901445(23)	5.554750(18)	342.297(1)
380.0	7.800554(20)	7.902590(23)	5.554899(18)	342.429(1)
400.0	7.802230(20)	7.903732(23)	5.554969(18)	342.557(1)
420.0	7.804004(21)	7.904913(24)	5.555137(18)	342.696(1)
Andalusite series two (And + NIST silicon, Al slab can, CCR)				
290.0	7.793211(19)	7.897698(24)	5.554523(20)	341.872(1)
295.65	7.793643(19)	7.897985(23)	5.554549(20)	341.905(1)
310.0	7.794772(20)	7.898723(24)	5.554548(21)	341.987(1)

320.0	7.795641(19)	7.899275(24)	5.554554(20)	342.049(1)
330.0	7.796431(19)	7.899794(24)	5.554625(20)	342.110(1)
350.0	7.798041(20)	7.900880(24)	5.554702(21)	342.233(1)
370.0	7.799766(19)	7.901979(24)	5.554762(20)	342.360(1)
390.0	7.801467(20)	7.903156(24)	5.554915(21)	342.495(1)
410.0	7.803214(20)	7.904419(24)	5.555058(21)	342.635(1)
430.0	7.805067(20)	7.905645(25)	5.555186(22)	342.778(1)

Andalusite series three (And, vanadium cylinder, furnace)

370.2	7.800112(24)	7.902194(22)	5.554797(14)	342.387(1)
423.6	7.804822(23)	7.905361(21)	5.555147(13)	342.752(1)
473.6	7.809831(25)	7.908845(23)	5.555652(14)	343.154(1)
523.4	7.814818(24)	7.912388(23)	5.556163(14)	343.559(1)
573.3	7.819940(26)	7.915913(25)	5.556718(15)	343.972(1)
623.2	7.824975(24)	7.919634(23)	5.557400(14)	344.397(1)
673.0	7.830229(25)	7.923311(23)	5.557982(14)	344.825(1)
723.0	7.835320(25)	7.927024(23)	5.558697(14)	345.255(1)
772.9	7.840545(24)	7.930820(22)	5.559402(14)	345.694(1)
822.7	7.845709(27)	7.934632(24)	5.560096(14)	346.132(1)
872.4	7.850872(28)	7.938421(25)	5.560822(15)	346.570(1)
921.8	7.856005(30)	7.942217(25)	5.561548(16)	347.008(1)
971.5	7.861182(32)	7.946110(26)	5.562292(17)	347.453(1)
1021.5	7.866501(33)	7.950076(26)	5.563036(18)	347.908(1)
1071.6	7.871960(34)	7.954194(26)	5.563834(18)	348.380(1)
1121.8	7.877533(34)	7.958369(27)	5.564636(18)	348.860(1)
1171.8	7.883062(32)	7.962564(27)	5.565478(17)	349.342(1)
1222.2	7.888448(30)	7.966721(26)	5.566320(16)	349.816(2)
1272.3	7.893972(31)	7.971070(28)	5.567194(17)	350.307(2)
1322.0	7.899474(32)	7.975376(30)	5.568030(18)	350.793(2)
1371.7	7.905086(29)	7.979721(27)	5.568900(17)	351.288(1)
1422.0	7.910640(32)	7.984114(30)	5.569743(18)	351.782(2)
1472.5	7.916265(34)	7.988549(32)	5.570547(20)	352.278(2)
1522.8	7.921866(33)	7.993023(31)	5.571311(19)	352.774(2)
1573.0	7.927555(28)	7.997695(26)	5.572002(16)	353.277(1)

Table S5:

Refined lattice parameters of sillimanite

T (K)	*a* (Å)	*b* (Å)	*c* (Å)	V (Å^3)
Sillimanite series one (Sil, Al slab-can, CCR)				
10.0	7.487913(36)	7.668875(11)	5.771073(20)	331.397(2)
20.0	7.487936(43)	7.668880(13)	5.771040(24)	331.397(2)
30.0	7.487835(44)	7.668900(13)	5.771052(24)	331.394(2)
40.0	7.487861(45)	7.668920(14)	5.771020(25)	331.394(2)
50.0	7.487855(45)	7.668943(14)	5.771078(25)	331.398(2)
60.0	7.487763(43)	7.668969(13)	5.771075(24)	331.395(2)
70.0	7.487741(45)	7.669025(14)	5.771058(25)	331.395(2)
80.0	7.487622(44)	7.669117(13)	5.771004(24)	331.391(2)
90.0	7.487552(44)	7.669177(14)	5.771078(25)	331.395(2)
100.0	7.487394(44)	7.669306(13)	5.771047(24)	331.392(2)
110.0	7.487318(45)	7.669421(14)	5.771038(25)	331.393(2)
120.0	7.487353(44)	7.669573(14)	5.771049(24)	331.401(2)
130.0	7.487099(44)	7.669786(14)	5.771022(24)	331.398(2)
140.0	7.487123(44)	7.669925(14)	5.771080(24)	331.408(2)
150.0	7.487001(45)	7.670183(14)	5.771077(25)	331.414(2)
160.0	7.486838(45)	7.670407(14)	5.771152(25)	331.421(2)
170.0	7.486857(45)	7.670643(14)	5.771145(25)	331.431(2)
180.0	7.486725(46)	7.670940(14)	5.771231(25)	331.443(2)
190.0	7.486633(46)	7.671219(14)	5.771305(25)	331.455(2)
200.0	7.486567(44)	7.671536(13)	5.771355(24)	331.469(2)
220.0	7.486440(48)	7.672171(15)	5.771537(26)	331.501(2)
240.0	7.486493(45)	7.672893(14)	5.771697(25)	331.544(2)
260.0	7.486351(45)	7.673636(14)	5.771922(25)	331.583(2)
280.0	7.486485(45)	7.674419(14)	5.772168(25)	331.637(2)
295.65	7.486443(47)	7.675086(14)	5.772468(25)	331.681(2)
300.0	7.486384(46)	7.675287(14)	5.772517(25)	331.690(2)
320.0	7.486370(46)	7.676151(14)	5.772861(26)	331.746(2)
340.0	7.486546(48)	7.677081(15)	5.773179(27)	331.812(2)
360.0	7.486556(46)	7.678027(15)	5.773604(26)	331.878(2)
380.0	7.486796(44)	7.679014(14)	5.773916(24)	331.949(2)
400.0	7.486891(47)	7.680019(15)	5.774313(26)	332.020(2)
420.0	7.487073(45)	7.681058(14)	5.774770(25)	332.099(2)
440.0	7.487220(45)	7.682110(14)	5.775204(25)	332.176(2)
Sillimanite series two (Sil + NIST silicon, Al slab can, CCR)				
290.0	7.486411(59)	7.674672(16)	5.772316(29)	331.653(3)

295.65	7.486427(47)	7.674904(14)	5.772490(24)	331.673(2)
370.0	7.486690(47)	7.678429(14)	5.773817(24)	331.914(2)

Sillimanite series three (Sil, vanadium cylinder, furnace)

370.2	7.486717(16)	7.678533(25)	5.773764(12)	331.916(1)
423.6	7.487141(22)	7.681039(34)	5.774773(15)	332.102(1)
473.6	7.487672(23)	7.684022(35)	5.776005(16)	332.325(1)
523.4	7.488276(22)	7.686954(35)	5.777321(16)	332.554(1)
573.3	7.488998(23)	7.690148(36)	5.778707(16)	332.804(1)
623.2	7.489787(23)	7.693391(36)	5.780117(16)	333.061(1)
673.0	7.490670(23)	7.696648(37)	5.781559(16)	333.324(1)
723.0	7.491535(24)	7.699906(38)	5.782985(17)	333.586(2)
772.9	7.492484(24)	7.703200(38)	5.784513(17)	333.860(2)
822.7	7.493443(25)	7.706615(39)	5.785985(17)	334.135(2)
872.4	7.494508(24)	7.709962(38)	5.787557(17)	334.419(2)
921.8	7.495573(24)	7.713432(38)	5.789060(17)	334.704(2)
971.5	7.496656(25)	7.716832(39)	5.790637(18)	334.991(2)
1021.5	7.497757(24)	7.720345(38)	5.792208(17)	335.284(2)
1071.6	7.498909(24)	7.723895(39)	5.793800(17)	335.581(2)
1121.8	7.500120(25)	7.727458(40)	5.795420(18)	335.884(2)
1171.8	7.501274(26)	7.731035(42)	5.797064(18)	336.187(2)
1222.1	7.502476(27)	7.734866(42)	5.798674(19)	336.501(2)
1272.3	7.503772(27)	7.738912(43)	5.800332(18)	336.831(2)
1322.0	7.505140(29)	7.742991(45)	5.801972(20)	337.166(2)
1371.7	7.506594(28)	7.747329(44)	5.803546(19)	337.511(2)
1422.0	7.507985(29)	7.751659(47)	5.805139(20)	337.855(2)
1472.5	7.509453(28)	7.756234(45)	5.806689(19)	338.211(2)
1522.8	7.511109(29)	7.760867(47)	5.808196(19)	338.576(2)
1573.0	7.512864(29)	7.766186(48)	5.809564(20)	338.967(2)

Table S6

Triple-Debye model fit to experimental heat capacities

	kyanite	andalusite	sillimanite
X	0.51(1)	0.391(5)	0.378(5)
θ_{D1} (K)	684 ± 7	532 ± 3	498 ± 3
Y	0.51(1)	0.622(4)	0.616(4)
θ_{D2} (K)	1360 ± 17	1297 ± 6	1267 ± 8
Z	0.44(5)	0.37(4)	0.47(5)
θ_{D3} (K)	9807 ± 552	10024 ± 521	9331 ± 505
R^2	99.9983 %	99.9990 %	99.9956 %
Max residual ($J\ mol^{-1}\ K^{-1}$)	1.6	1.2	1.2

Table S7

Parameters derived from partial fitting of a triple-Debye model to the unit-cell volumes of the three Al_2SiO_5 polymorphs. Parameters that were fixed on the basis of fitting to the heat capacity or literature values for the bulk modulus are in plain type; parameters that were allowed to vary are in bold.

	kyanite	andalusite	sillimanite*
X	**0.543(8)**	**0.398(5)**	**−0.034(3)**
θ_{D1} (K)	683.6	531.6	497.8
Y	**0.62(1)**	**0.659(8)**	**0.814(5)**
θ_{D2} (K)	1359.6	1296.9	1267.2
Z	**0.66(4)**	**0.20(3)**	**0.11(4)**
θ_{D3} (K)	9807.4	10023.9	9331.3
Q (J cm^{-3})	8.5057x10^6	7.4055x10^6	8.1825x10^6
K_0 (GPa)	193.0[a]	144.2[b]	164[b]
V_0 (cm^3 mol^{-1})	44.0720	51.3553	49.8930
V_0 (Å^3)	292.7331	341.1099	331.3970
R^2	99.9981 %	99.9977 %	99.9406 %
Max residual (Å^3)	0.062	0.042	0.015

*Fitted over the range 10–1200 K

[a]Yang et al. (1997a, 1997b)

[b]Burt et al. (2006)

Table S8

Parameters obtained from fitting Eq. 1 to the unit-cell parameters of kyanite in the range 10 – 1573 K. Units for X_0 and the residuals are Å, degrees or Å^3 as appropriate. The term S is defined by Eqs. 2–5 in the main text. Values are reported here to more significant figures than Table 2 in the main text.

	a-axis	*b*-axis	*c*-axis	Volume
	S = A	S = A	S = A	S = A
X_0	7.116100	7.843899	5.569062	292.73388
a	7.3516×10^{-5}	7.0795×10^{-5}	6.7030×10^{-5}	9.3740×10^{-3}
b	−78.935	−76.893	−75.739	−78.482
	α	β	γ	
	S = A	quadratic	linear	
X_0	89.992022	101.122882	106.002159	
a	-1.0383×10^{-4}	1.6849×10^{-5}	2.6904×10^{-6}	
b	−29.427	-1.4131×10^{-8}	–	

Table S9

Parameters obtained from fitting Eq. 1 to the unit-cell parameters of andalusite in the range 10 – 1573 K. Units for X_0 and the residuals are Å, degrees or Å^3 as appropriate. The term S is defined by Eqs. 2–5 in the main text. Values are reported here to more significant figures than Table 3 in the main text.

	a-axis S = A	*b*-axis S = A	*c*-axis S = A + B	Volume S = A
X_0	7.780928	7.890853	5.555640	341.10236
a	1.1954×10^{-4}	9.3866×10^{-5}	-5.6098×10^{-5}	1.0790×10^{-2}
b	−52.441	−70.169	−61.903	−70.683
c	–	–	7.2156×10^{-5}	–
d	–	–	−500.828	–

Table S10

Parameters obtained from fitting Eq. 1 to the unit-cell parameters of sillimanite in the range 10 – 1177 K. Units for X_0 and the residuals are Å, degrees or Å^3 as appropriate. The term S is defined by Eqs. 2–5 in the main text. Values are reported here to more significant figures than Table 4 in the main text.

	a-axis S = A + B	*b*-axis S = A	*c*-axis S = C	Volume S = B
X_0	7.487920	7.668990	5.771076	331.39188
a	-1.7253×10^{-5}	8.1995×10^{-5}	3.2522×10^{-5}	6.7048×10^{-3}
b	−27.470	−72.143	388.859	−575.441
c	4.5245×10^{-5}	–	–	–
d	−648.778	–	–	–

Figure S1:

Raman spectra of the mineral specimens used in this work (black) compared with RRUFF library spectra (red). Spectra were measured at a power of 40 mW (at the probe tip) for 30 s kyanite), 60 s (andalusite) and 50 s (sillimanite). Spectra are reproduced by permission of the RRUFF project (Lafuente et al., 2015).

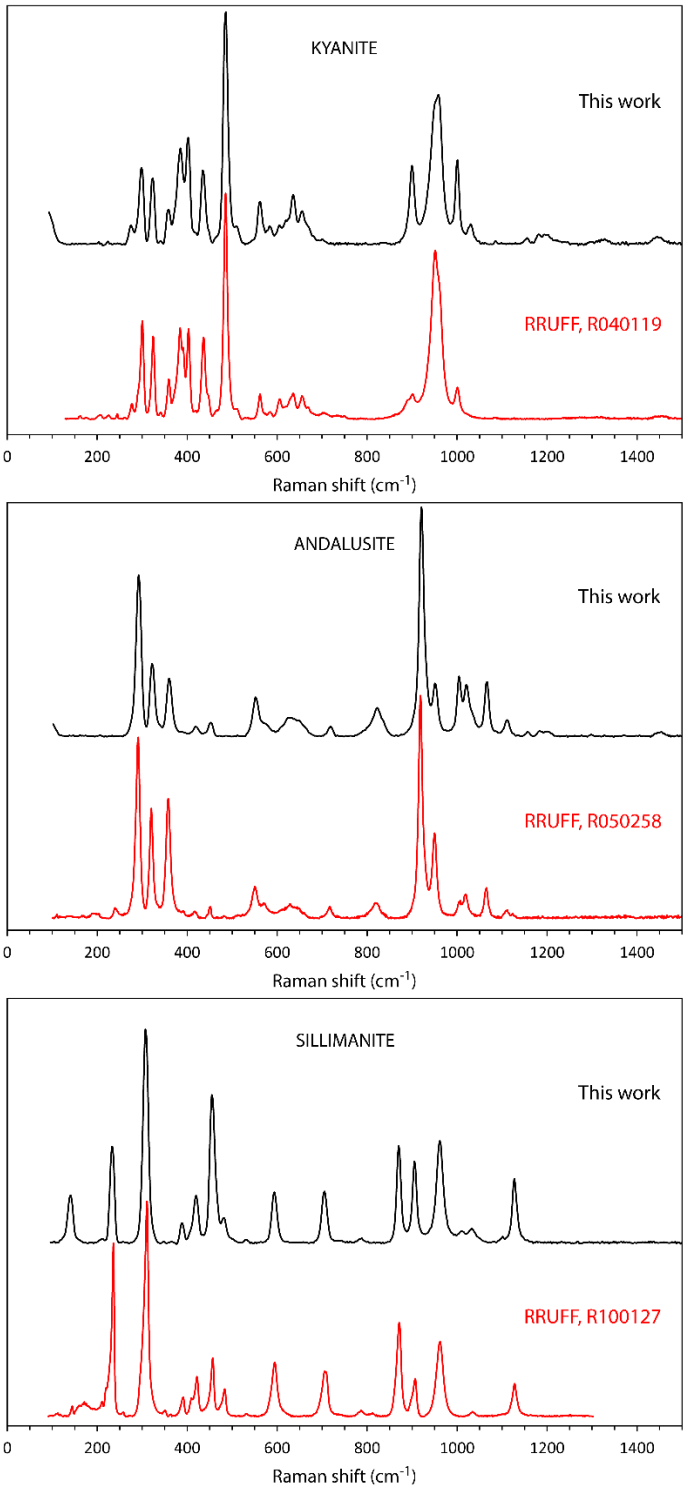

Figure S2:

Stereographic inverse pole figures along *001* at 300 K in the slab-geometry sample holder: (a) kyanite; (b) andalusite; (c) sillimanite. Shading and contours report values in multiples of a random distribution (MRD) computed from the texture coefficients, C_L^{mn}, given in Table S1.

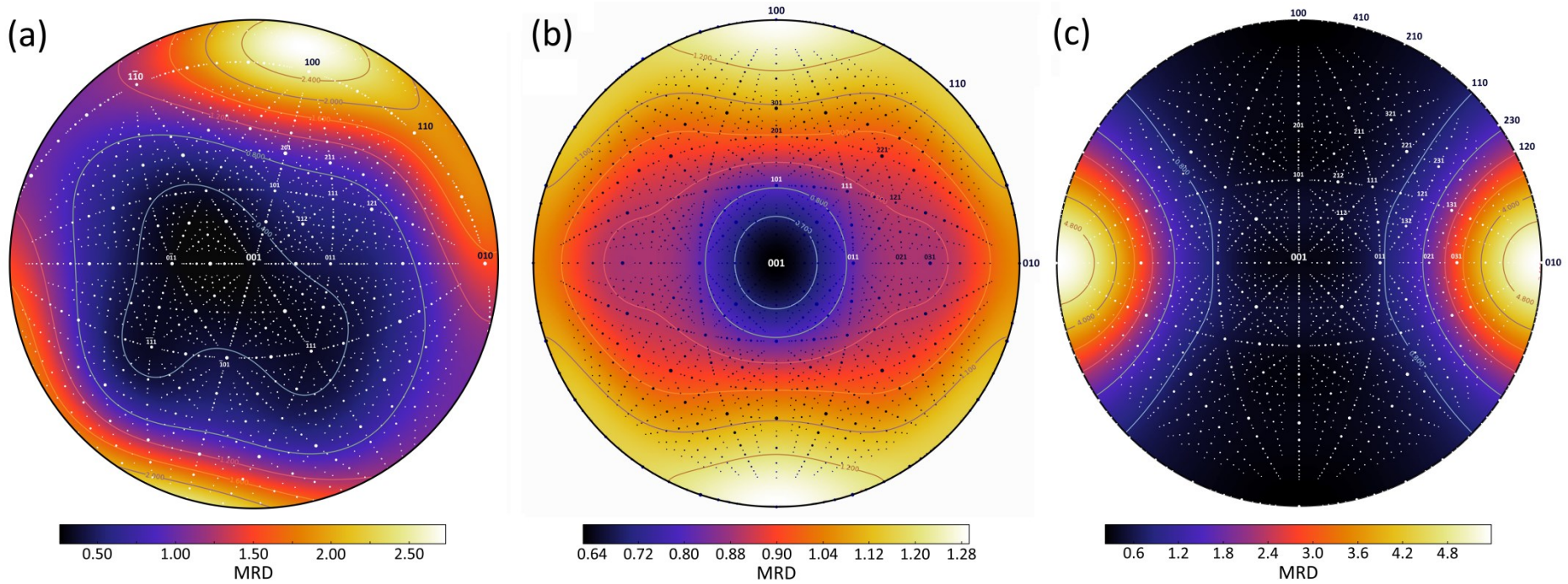

Figure S3:

Lattice parameters of kyanite as a function of temperature (< 600 K); solid black lines represent the fit of a simplified model described in the main text (Eq. 1).

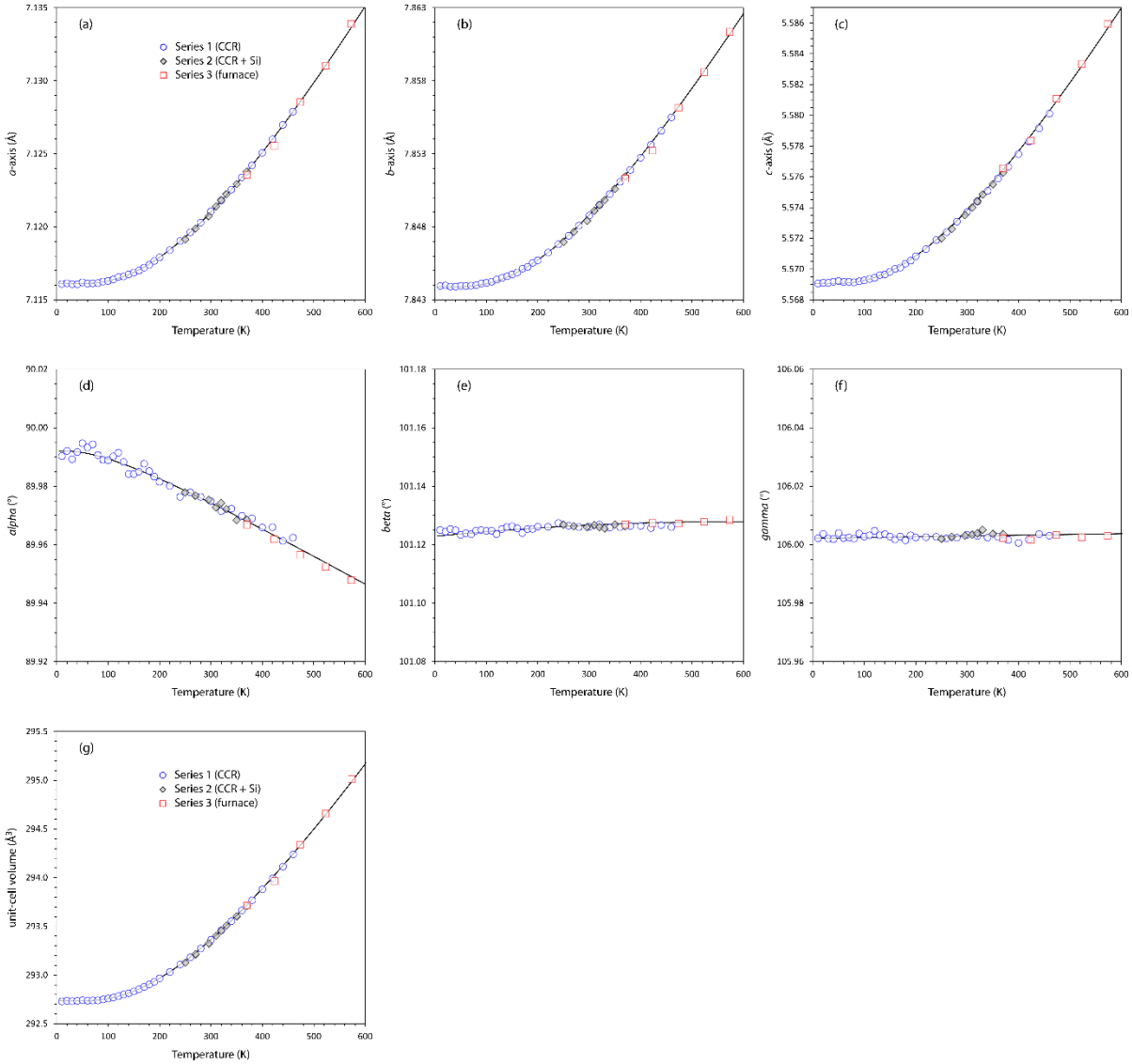

Figure S4:

Lattice parameters and axial ratios of andalusite as a function of temperature (< 600 K); solid black lines represent the fit of a simplified model described in the main text (Eq. 1).

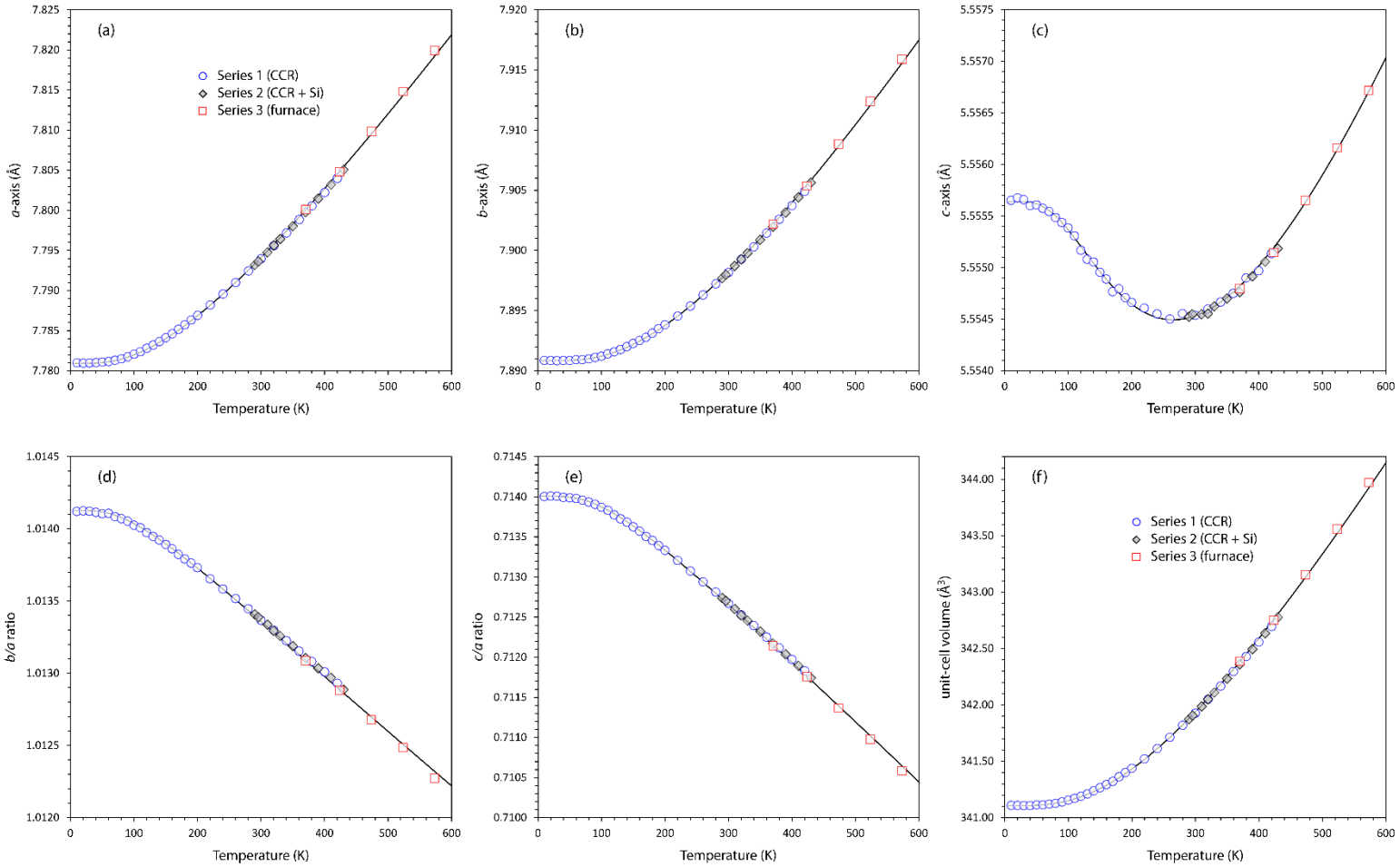

Figure S5:

Lattice parameters and axial ratios of sillimanite as a function of temperature (< 600 K); solid black lines represent the fit of a simplified model described in the main text (Eq. 1).

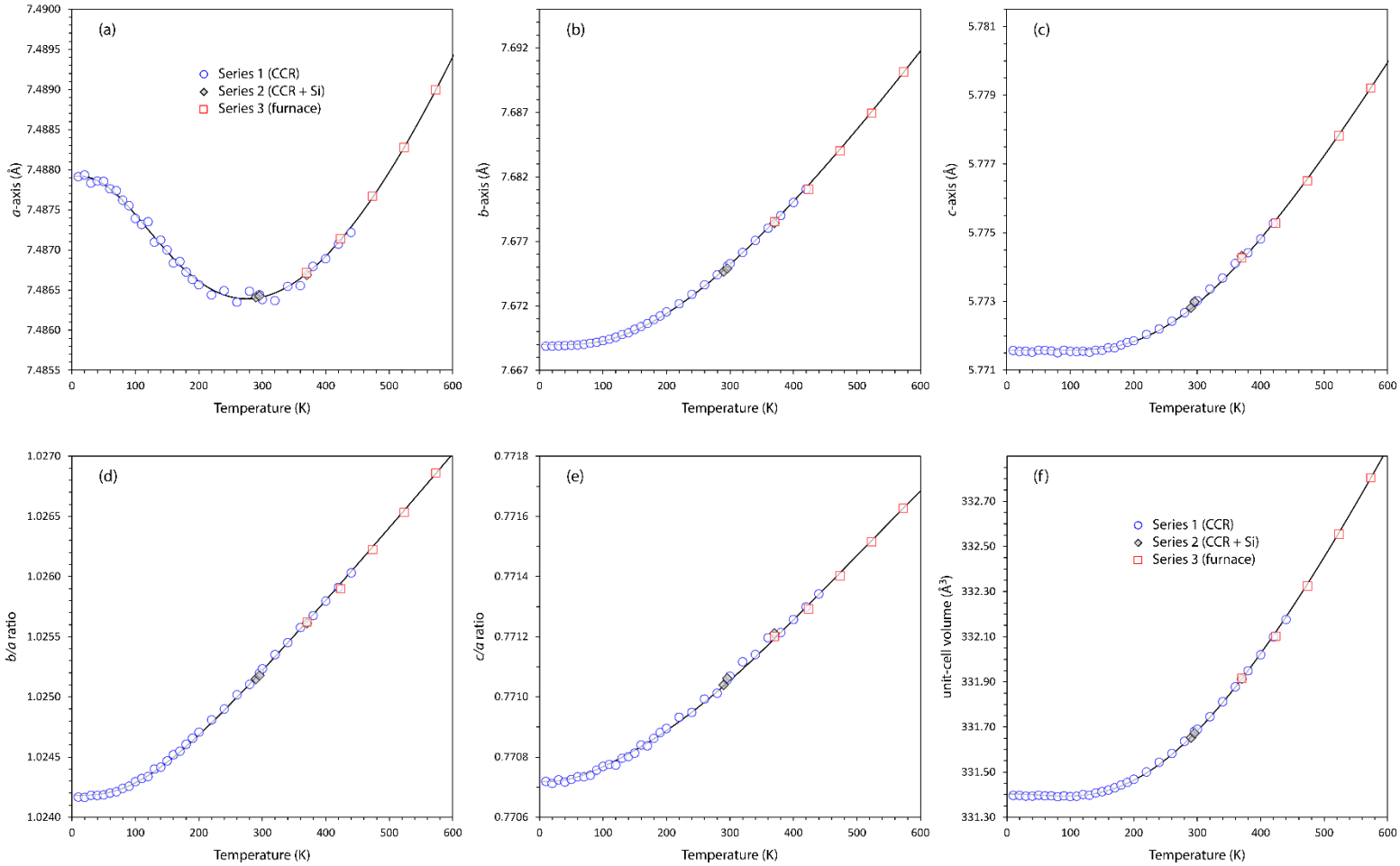

Figure S6:

Fits of triple-Debye models to the heat capacities of (a) kyanite, (b) andalusite and (c) sillimanite. Symbols represent the ensemble of all experimental data (see text below) and the red lines are the model fit. The contribution from the first two Debye terms is shown in each case by the dashed line.

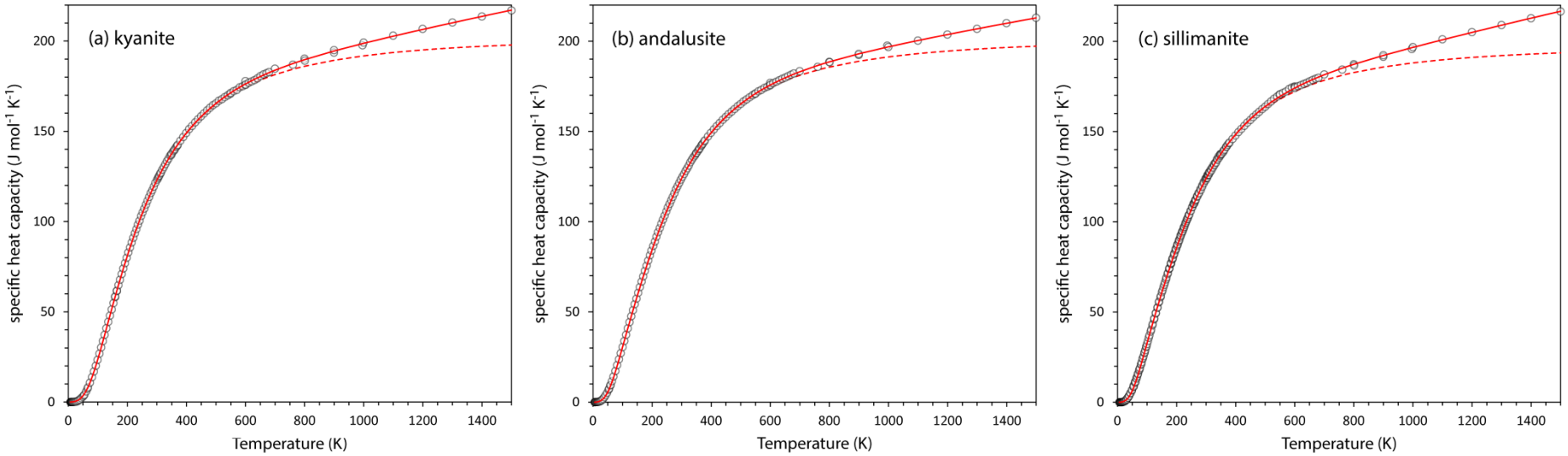

Figure S7:

Temperature dependences of the molar volume difference between each set of polymorph pairs. Lines and symbols have the same meaning as Figures S3 – S5.

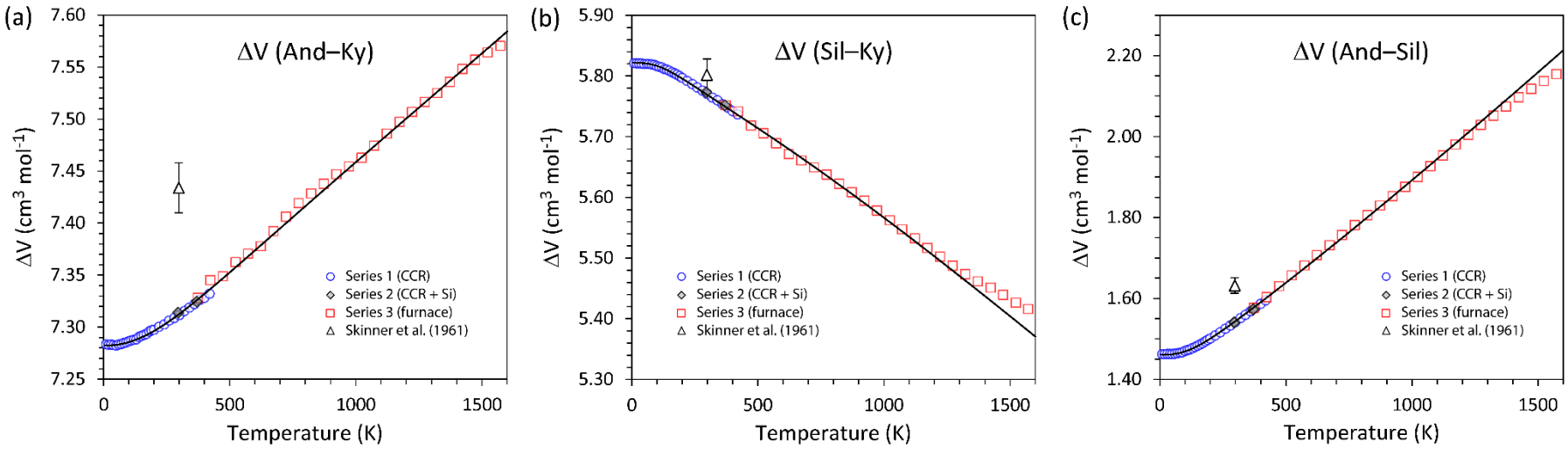

Triple-Debye model fit to the heat capacities and unit-cell volumes

The molar volume of a crystal may be parameterised in a physically-meaningful way using a Debye model of the internal energy to first order:

$$V(T) = V_0\left(1 + \frac{U(T)}{Q}\right) \quad \text{(S1)}$$

where V_0 is the volume at zero Kelvin and $Q = V_0K_0/\gamma$ with the assumption that the bulk modulus, K_0, and the Grüneisen parameter, γ, are both independent of temperature. The internal energy of the crystal, *U(T)* is obtained from a Debye approximation of the vibrational density of states (Cochran, 1973):

$$U(T) = 9Nk_BT\left(\frac{T}{\theta_D}\right)^3\int_0^{\frac{\theta_D}{T}}\frac{x^3}{e^x - 1}dx \quad \text{(S2)}$$

N is the number of atoms in the unit cell, k_B is Boltzmann's constant, θ_D is the characteristic Debye temperature, and $x = \hbar\omega/k_BT$. The most accurate determination of *U(T)* is obtained by fitting of a Debye-type model to the heat capacity; since this internal energy typically reflects contributions from a broad spectrum of vibrational modes it is often the case that more than one Debye function is necessary to achieve the optimum agreement between the model and the observations. In this instance, it was found that a model containing three Debye functions was needed:

$$C = 9Nk_B\left[Xf\left(\frac{\theta_{D1}}{T}\right) + Yf\left(\frac{\theta_{D2}}{T}\right) + Zf\left(\frac{\theta_{D3}}{T}\right)\right] \quad \text{(S3)}$$

where $f(\theta_D/T)$ is the Debye function and X, Y and Z are scaling factors. This model was fitted to literature values of the isobaric heat capacity, C_P (Pankratz & Kelley, 1964; Robie & Hemingway, 1984; Salje, 1986; Hemingway et al., 1991) to yield the parameters listed in Supplementary Table S6 and the fits shown in Figure S6. The contribution from the first two Debye-terms, which might be thought of as the harmonic part of the specific heat, saturates very close to the classical Dulong-Petit limit (dashed lines in Figure S6) whereas the monotonic increase in the heat capacity above 800 K from the third Debye-term may be thought of as the quasi-harmonic component. The contribution of the third Debye term is

comparatively small up to 1600 K, since the values of $\theta_{D3}$are so large, and thus the magnitude of the scale factor *Z* is not physically meaningful.

The vibrational densities of states (VDOS) of each mineral has been measured using inelastic neutron spectroscopy (Rao et al., 1999, 2002; Goel et al., 2002), allowing us to draw some comparisons between the Debye cut-offs obtained from fitting the heat capacity with the real vibrational spectrum. Each mineral, roughly speaking, has a similar spectrum with broad clump of modes below 100 meV (displaying varying degrees of structure), a small gap and then a sharper group of modes in 110–135 meV range. The gap near 100 meV is clearest in andalusite and least clear in sillimanite. My Debye model fits all have θ_{D2} in the range 1260 – 1360 K, corresponding to energies of 109 – 117 meV (875 – 945 cm^{-1}), in good agreement with the obvious cut-offs in the measured vibrational spectra. The only mineral with a clean, sharp cut-off at lower energies is andalusite (Rao et al., 2002) where a feature that may be correlated with θ_{D1} = 532 K = 46 meV is observed.

The three-Debye model of the internal energy was then used as the basis for fitting the molar volumes of each polymorph (Eq. S1), keeping the Debye temperatures fixed. Estimates of *Q* were derived using the measured bulk moduli (Yang et al., 1997a, 1997b; Burt et al., 2006), assuming $\gamma = 1$. In practice, the scaling factors accommodate any deviation of γ from unity and, importantly, any deviation from a positive value. Thus *X*, *Y* and *Z* in the molar volume fits are inversely proportional to the Grüneisen parameters of the vibrational modes corresponding with θ_{D1}, θ_{D2} and θ_{D3}, respectively. Allowing only the scale factors of the Debye functions to vary resulted in excellent fits of the molar volumes, including the slight region of negative volume expansion in sillimanite at low temperature. The complete set of parameters used in each model is reported in Supplementary Table S6.

There are two noteworthy observations to be made regarding this model fit. First, the frequency spectrum obtained from the specific heats, combined with the observed bulk elastic stiffnesses and molar volumes, leads to an excellent representation of the thermal expansion via Eq. S1. Secondly, the negative value of the scale factor *X* for sillimanite is an indication that the Grüneisen parameter for the low-frequency vibrational modes up to the θ_{D1} cut-off (498 K = 346 cm^{-1} = 43 meV) is negative. This agrees with measurements of the pressure-dependence of Raman-active vibrational modes by Mernagh & Liu (1991), who found Grüneisen parameters of −0.48(5) for the peak observed (at zero *P*) at 311 cm^{-1} and γ = −0.92(9) for the Raman peak at 236 cm^{-1}.

Literature cited in this Supplement

Burt, J.B., Ross, N.L., Angel, R.J., & Koch, M. (2006) Equations of state and structures of andalusite to 9.8 GPa and sillimanite to 8.5 GPa. *American Mineralogist* **91**, 319–326.

Cochran, W. (1973) *The Dynamics of Atoms in Crystals.* Arnold, London.

Goel, P., Rao, M. N., Choudhury, N., Chaplot, S. L., Ghose, S., & Yethiraj, M. (2002). Phonon-dispersion relations in andalusite and sillimanite, Al_2SiO_5. *Applied Physics A* **74**, s1149–s1151.

Hemingway, B.S., Robie, R.A., Evans, H.T., & Kerrick, D.M. (1991) Heat capacities and entropies of sillimanite, fibrolite, andalusite, kyanite, and quartz and the Al_2SiO_5 phase diagram. *American Mineralogist* **76**, 1597–1613.

Lafuente, B., Downs, R. T., Yang, H., & Stone, N. (2015) The power of databases: the RRUFF project. In: *Highlights in Mineralogical Crystallography* (T. Armbruster and R. M. Danisi, Eds), Berlin, Germany, W. De Gruyter, pp 1–30.

Mernagh, T. P., Liu, L. (1991) Raman spectra from the Al_2SiO_5 polymorphs at high pressure and room temperature. *Physics and Chemistry of Minerals* **18**, 126–130.

Pankratz, L.B., & Kelley, K.K. (1964) High temperature heat contents and entropies of andalusite, kyanite and sillimanite. *U. S. Bur. Mines Rep. Invest*.6370.

Rao, M. N., Chaplot, S. L., Choudhury, N., Rao, K. R., Azuah, R. T., Montfrooij, W. T., & Bennington, S. M. (1999) Lattice dynamics and inelastic neutron scattering from sillimanite and kyanite Al_2SiO_5. *Physical Review B* **60**, 12061–12068.

Rao, M. N., Goel, P., Choudhury, N., Chaplot, S. L., & Ghose, S. (2002) Lattice dynamics and inelastic neutron scattering experiments on andalusite, Al_2SiO_5. *Solid State Communications* **121**, 333–338.

Robie, R.A., & Hemingway, B.S. (1984) Entropies of kyanite, andalusite, and sillimanite: additional constraints on the pressure and temperature of the Al_2SiO_5 triple point. *American Mineralogist* **69**, 298–306.

Salje, E. (1986) Heat capacities and entropies of andalusite and sillimanite: the influence of fibrolitization on the phase diagram of the Al_2SiO_5 polymorphs. *American Mineralogist* **71**, 1366–1371.

Yang, H., Downs, R.T., Finger, L.W., Hazen, R.M., & Prewitt, C.T. (1997a) Compressibility and crystal structure of kyanite, Al_2SiO_5, at high pressure. *American Mineralogist* **82**, 467–474.

Yang, H., Hazen, R.M., Finger, L.W., Prewitt, C.T., and Downs, R.T. (1997b) Compressibility and crystal structure of sillimanite, Al_2SiO_5, at high pressure. *Physics and Chemistry of Minerals* **25**, 39–47.